Farfield Plume Measurement and Analysis on the NASA-300M

Wensheng Huang, Rohit Shastry, George C. Soulas, and Hani Kamhawi
National Aeronautics and Space Administration Glenn Research Center
Cleveland, Ohio, 44135

ABSTRACT

NASA is developing a 15-kW Hall thruster to support future NASA missions. This activity is funded under the Space Technology Mission Directorate Solar Electric Propulsion Technology Demonstration project. As a part of the development process, the far-field plume characteristics of the NASA-300M, a 20-kW Hall thruster, were studied. The results will be used to study how various aspects of the operation of this thruster affect the overall performance. This data will be used to guide future design work and serve as a baseline for comparison to a magnetically shielded version of the NASA-300M that will be tested in the future. For this study, a far-field Faraday probe was swept in a polar fashion to map the ion current density. An ExB probe (Wien filter), two retarding potential analyzers, and a Langmuir probe were mounted at a fixed location on the thruster axis in the far-field plume. The data reduction method followed recommendations in recent studies by Brown, Reid, and Shastry with modifications that are tailored to the plasma plume environment of high-power Hall thrusters. Results from this and prior testing show that the plume is richer in doubly-charged ions, larger in spatial extent, and capable of greater probe heating than lower power thrusters. These characteristics require special treatment in experimental setup and data analysis, which will be the main focus of this paper. In particular, covered topics will include a new, more accurate, method of integration for analysis of the ExB probe data and effect of secondary electron emission on the Faraday probe data.

ABBREVIATIONS

GRC = Glenn Research Center
HEFT = Human Exploration Framework Team
STMD = Space Technology Mission Directorate
ISP = In Space Propulsion
300M = NASA-300M
300MS = NASA-300MS
RPA = Retarding Potential Analyzer
CEX = Charge-exchange
SEE = Secondary Electron Emission
MTD = Mean Thruster Diameter

I. INTRODUCTION

In 2010, NASA established the Human Exploration Framework Team (HEFT) to analyze exploration and technology concepts and provide inputs to the agency's senior leadership on the key components of a safe, sustainable, affordable, and credible future human space exploration endeavor for the nation.[1] The team concluded, in part, that the use of a high power (i.e. on the order of 300 kW) solar electric propulsion system could significantly reduce the number of heavy lift launch vehicles required for a human mission to a near earth asteroid.[1,2] Hall thrusters were found to be ideal for such applications because of their high power processing capabilities and their efficient operation at moderate specific impulses, which leads to reduced trip times that are necessary for such missions.[2-4] Recent electric propulsion system model estimates that considered factors such as cost, mass, fault-tolerance, cost uncertainty, complexity, ground test vacuum facility limitations, previously demonstrated power capabilities, and possible technology limitations have shown that Hall thrusters operating at power levels of 20-50 kW are strong candidates for human exploration missions operating at total powers up to 500 kW.[2,5]

As an intermediate step towards the aforementioned higher power Hall thruster, the Space Technology Mission Directorate (STMD) is investing in the development of a 15-kW Hall thruster. This thruster will serve as a stepping stone to higher power and provide a state-of-the-art propulsion system for the Solar Electric Propulsion (SEP) Technology Demonstration Mission (TDM). SEP TDM, initially announced in 2011, is aimed at demonstrating new cutting edge technology in solar arrays, spacecraft bus, and electric propulsion that will increase the maturity of these SEP technologies for future commercial use. Once these technologies have been demonstrated, they are expected to enable higher performance low-Earth orbit to geosynchronous Earth orbit (LEO to GEO) transfers as well as a number of other near-Earth orbit transfers and station-keeping maneuvers. In longer terms, these technologies will reduce mission costs for NASA interplanetary missions and will serve as a precursor to higher power systems for manned interplanetary exploration.

The NASA Glenn Research Center (GRC) is partnering with the Jet Propulsion Laboratory (JPL) to study high power Hall thrusters and obtain data for designing the aforementioned 15-kW Hall thruster. One of the activities prior to the design and fabrication of the 15-kW Hall thruster will be a set of studies comparing the NASA-300M, a 20-kW laboratory Hall thruster, with a magnetically-shielded version of the same thruster called the NASA-300MS. The NASA-300M was developed from 2004 to 2005 for project Prometheus but was not tested until recently due to project cancellation.[6] With the recent renewal in interest towards high-power Hall thrusters, the performance of the NASA-300M was characterized in 2010.[6] The study that will be described in this paper was a far-field probe interrogation of the 300M plasma plume. Information obtained from this study will form the baseline for comparison with the 300MS in a future study. These studies combined with the modeling effort by JPL will help confirm the principles of magnetic shielding when scaled up to power levels above 10 kW.

For this study, a far-field Faraday probe was swept in a polar fashion to map the ion current density. An electric-field-cross-magnetic-field (ExB) probe, also known as a Wien filter, two retarding potential analyzers (RPAs), and a Langmuir probe were mounted at a fixed location on the thruster axis in the far-field plume. The ExB probe was used to measure species fraction of the multiply-charged xenon species as compared to singly-charged xenon; the RPAs were used to measure energy per charge information of the plume; and the Langmuir probe was used to correct the RPA data. One of the RPA is newly designed by the Air Force Research Laboratory (AFRL) and was being validated.

The main focus of this paper will be on the experimental setup and modifications to traditional data analysis methods that came about as a result of special characteristics of high-power Hall thruster plumes. The data reduction methods are based on recent studies by Brown,[7] Reid,[8] and Shastry[9] with modifications that are tailored to the plasma plume environment of high-power Hall thrusters. Results from this and prior testing show that the plume is richer in doubly-charged ions, larger in spatial extent, and capable of greater probe heating than lower power thrusters. These characteristics require special treatment in experimental setup and data analysis, which will be the main focus of this paper. In particular, covered topics will include a new, more accurate, method of integration for analysis of the ExB probe data and effect of secondary electron emission on the Faraday probe data. The test methodology and data analysis carried out for this paper draws heavily from the knowledge gained during those tests.

II. EXPERIMENTAL SETUP

For the sake of brevity and to simplify plot labeling, NASA-300M will sometimes be referred to as the 300M in this paper. Operating conditions are labeled as www V, yy.y A, where www is the discharge voltage in volts and yy.y is the discharge current in amperes. Unless otherwise noted, all spatial positions presented in this paper have been normalized by the mean thruster diameter of the thruster. Mean thruster diameter (MTD) is defined as the average of the inner and outer discharge-channel wall diameters.

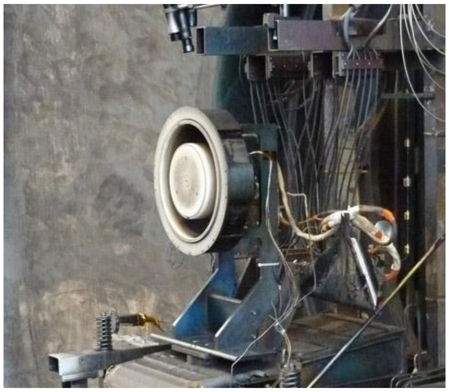

Figure 1. NASA-300M mounted on a thrust stand.

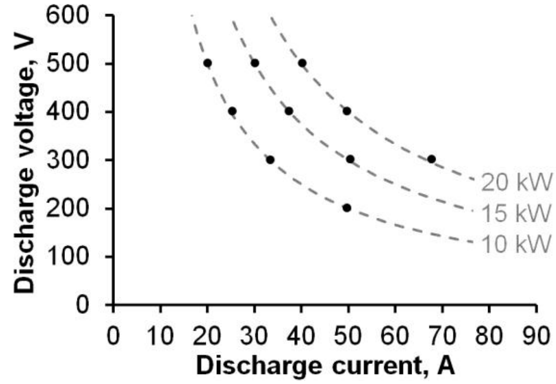

Figure 2. Operating conditions tested for this study.

A. Thruster, Thrust Stand, and Test Matrix

The NASA-300M is a magnetic-layer Hall thruster. It was designed based on the principles outlined in Manzella's dissertation work.[10] A photograph of the 300M mounted on the thrust stand is shown in Fig. 1. This thruster was originally developed for high-specific-impulse missions[6] and has lens-type magnetic field topology.[11,12] The thruster ran with a centrally-mounted hollow cathode derived from the discharge cathode for NASA's Evolutionary Xenon Thruster (NEXT).[6] For the data presented in this paper, the magnetic field settings of the thruster were optimized to give a shape roughly symmetric about the channel centerline while maximizing anode efficiency. The cathode flow fraction was 8%.

The nominal operating condition of NASA-300M is 500 V, 40 A. For this test, the 300M is operated at 10 conditions spanning discharge voltages of 200 to 500 V, discharge currents of 20 to 67 A, and discharge powers of 10 to 20 kW. The anode efficiency of this thruster, defined in Eq. (1), varies from 57 to 69% over the tested operating conditions.

$$\eta_a = \frac{T^2}{2\dot{m}_a I_d V_d} \quad (1)$$

In this equation, T is thrust, $\dot{m}_a$ is anode mass flow rate, I_d is discharge current, and V_d is discharge voltage. The boron nitride channel walls of the 300M have accumulated <110 hours of operation time prior to the start of this study.

The thrust stand used in this study is an inverted pendulum thrust stand designed by Haag.[13] It is actively cooled during operation. The nominal accuracy of this thrust stand is ±2%.[6] Long-term thermal drift is corrected by measuring the thrust signal with all gas flow to the thruster off and then assuming a linear change in the zero-thrust value over time. The maximum thermal drift was found to be no greater than 9 mN.

The throttling table for this study was designed to target a variety of discharge voltages in order to characterize the thruster for both high thrust-to-power (low specific impulse) and high specific impulse operation. Many of the conditions chosen also enable constant-current and constant-power comparisons. Figure 2 shows a diagram of all operating conditions tested for the present study of the 300M.

B. Vacuum Facility and Motion Stages

Testing was conducted in NASA GRC's Vacuum Facility 5. This cylindrical facility is 4.6 m in diameter and 18.3 m long and is pumped with a set of cryo-panels and 20 oil diffusion pumps. The 300M was mounted on a thrust stand in the main volume of the vacuum facility to ensure low pressures near the thruster during operation. Facility pressures were monitored with one Pirani gauge and six ion gauges, one of which is mounted next to the thrust stand. Facility pressure uncertainties were estimated

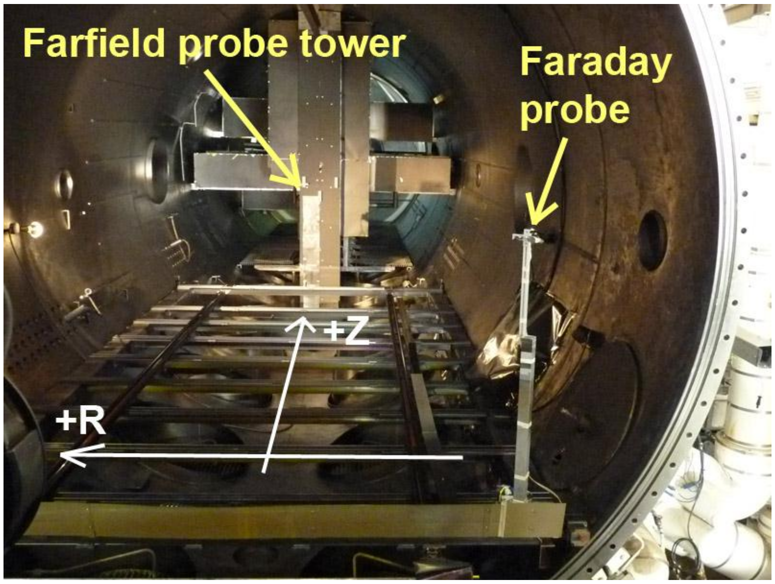

Figure 3. Photograph of the diagnostics setup.

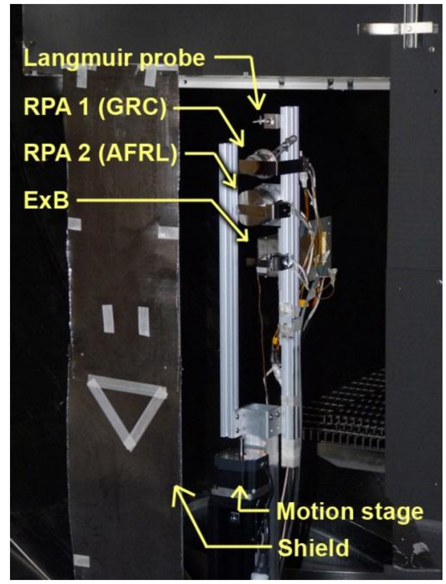

Figure 4. Photograph of the farfield probe tower.

by the manufacturer to be within ±6% of reading. The pressure reading, corrected for xenon, next to the thrust stand was less than 4.0×10^{-3} Pa (3.0×10^{-5} Torr) throughout testing.

A gas feed system made of commercially available components was used to feed xenon to the thruster. A 1000-sccm mass flow controller provides propellant to the anode while a 200-sccm controller provides propellant to the cathode. Both controllers were calibrated using xenon prior to testing. Typical uncertainties reported herein were ±1.0% of reading for the anode mass flow and ±1.1% of reading for total mass flows.

The commercial discharge power supply used is capable of supplying 2000 V at over 100 A with a 5.5 mF output filter capacitance. A 15.3 mF capacitor bank was connected in parallel with the power supply at the electrical feed-throughs of the vacuum facility to filter discharge current oscillations. In addition, separate commercial power supplies were used to power the cathode heater, cathode keeper, and electromagnets.

A farfield Faraday probe was mounted onto a commercially available three-axis belt-driven motion system. The motion system provides 2D rectilinear motion and probe rotation. Positioning accuracy is ~1 mm and <0.1°, respectively. Due to time constraints, data were only taken with the Faraday probe at 5 MTD away from the center of the thruster at exit plane. An ExB probe, two RPAs, and a Langmuir probe were mounted to a probe tower with accompanying shielding and shutters protecting the ExB probe and the RPAs. This farfield probe tower was attached to a vertical motion stage located ~27 MTD downstream of the thruster exit plane and positioned behind a Grafoil shield. During the data acquisition process, each probe was moved vertically to a point roughly along the central axis of the thruster before measurements were taken. The probe tower retreated behind the shield once data acquisition was completed. Figure 3 shows a photograph of the diagnostics setup. Figure 4 shows a photograph of the farfield probe tower.

C. Description of Probes and Data Acquisition System

This section will describe the probes used in this study in the following order, Langmuir probe, RPA, ExB probe, and Faraday probe. Unless otherwise stated, all probe biases were applied with commercial power supplies. The RPAs and ExB probe had leaf-blade shutters in front of them.

The Langmuir probe consists of a single tungsten wire protruding from an aluminum oxide tube. This probe was used to obtain the plasma potential at the same location as the RPA so that the RPA data can be corrected for this potential. This Langmuir probe was swept at 10 Hz for 1 second at each test point. The probe was connected to a custom circuit box where the probe current was passed through a shunt and the signal fed to an isolation amplifier. The bias voltage was passed through a voltage divider and fed to another isolation amplifier. Signal from the amplifiers were fed to a NI-9205 data acquisition module attached to a NI cDAQ-9178 unit.

Two four-grid RPAs were used in this study. These RPAs were used to approximate the average ion energy per charge. RPA 1 is of GRC design and was found based on prior experience to not work well at closer than ~25 MTD for medium to high power Hall thruster testing. For this reason, the probe tower was located at ~27 MTD from the thruster. RPA 2 is of AFRL design, courtesy of Daniel L. Brown and Joseph Blakely. For each RPA, the electron suppression and repelling grids were biased to -30 V with respect to facility ground while the ion retarding grid voltage was swept. The ion retarding grid was biased by a Keithley 2410 sourcemeter while the collected current was measured by a Keithley 6485 picoammeter. Results collected during the study show the two RPAs agree with each other and RPA 2 shows superior noise characteristics and stand-off against break down. Presented results will all be from RPA 2.

The ExB probe is a commercial product of Plasma Controls, LLC. It was used to measure charged species current fraction. The ExB probe weighs ~2 kg and is ~270 mm long. This ExB probe was the result of a Small Business Innovation Research project and has a proven history of usage.[14] Ions entering this ExB probe must first travel through a collimator, which ensures that the ions enter the ExB filter section along the probe axis. Perpendicular electric and magnetic fields then form the filter section where only charged particles of the right velocity can pass through to the electron suppression plate. A drift section separates the filter section and the electron suppression plate. The drift section enhances probe resolution and makes sure bias on the suppression plate does not affect the filter section. The electron suppression plate has a small orifice through which ions can pass through. It was biased at -30 V with respect to facility ground to suppress secondary electron emission from the collector. Ions passing through the suppression plate were collected by the collector. The collimator used in this study has an entrance and exit orifice diameter of 0.76 mm. The bias plates that form the electric field in the filter section have a gap distance of 3 mm. The electron suppression plate orifice diameter is ~1.5 mm. The collector is large enough to collect all ions that pass through the electron suppression plate orifice. A thermocouple was attached to the case of this ExB probe to make sure it did not overheat and de-magnetize. During testing, the main bias plate voltage was swept biased by a Keithley 6487 picoammeter, which also measured the collector current.

The Faraday probe, which is of GRC design, was used to measure ion current density. Figure 5 shows a cross-sectional diagram of this Faraday probe. The collector area is a circle of diameter 17.39 ± 0.02 mm. The front area of the collector is 238 mm^2. The probe has an overall diameter of ~28 mm. The collector and guard ring are made of molybdenum (to minimize secondary electron emission) and the insulating back is made of Macor. The collector and guard ring connections are mated to wires behind the insulating back and covered with fiberglass tape. The Faraday probe was set at 5 MTD away from the thruster because it needed to be far enough away from the thruster for the source of the thruster exhaust to be considered a point source. At the same time, the probe cannot be set too far away due to the effects of charge-exchange (CEX) between plume ions and background neutrals. During testing, the probe was set to different bias voltages (-20 to -40 V), and -30 V with respect to facility ground was selected to ensure electrons were properly repelled but sheath expansion was negligible. Collected current was measured via a shunt and an isolation amplifier. The output of the amplifier was fed to another NI-9205 data acquisition module attached to the aforementioned NI cDAQ-9178 unit.

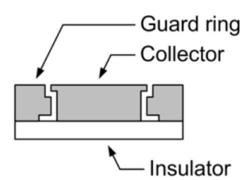

Figure 5. Diagram of the farfield Faraday probe.

The experiment was conducted via a dedicated data acquisition computer, which was running a custom Labview program. The motion stages were controlled by a motion controller that received movement commands from the computer. Encoder signals from the stages were fed into an encoder controller, which reports to the computer. The NI cDAQ-9178 data acquisition device and the various Keithley devices fed data to and were commanded by the computer. During the experiment, the computer automatically orchestrated the sequence of events that activated the various motion stages, shutters, and probes.

III. DATA REDUCTION

Data reduction was carried out in a specific sequence because, for the most part, each step of the analysis depended on the data obtained in the preceding steps. Though some of the analysis steps can be carried out independently, the accuracy of the result is decreased. For this study, the data analysis sequence is as follows, Langmuir probe analysis, RPA analysis, ExB probe analysis, and Faraday probe analysis. Additionally, pressure data is analyzed to help correct the ExB probe data for facility-background CEX effects. Differences between the presented data reduction procedures and traditional approaches will be highlighted with explanations for the rationale behind the new procedures.

A. Langmuir Probe Analysis

Langmuir probe analysis was carried out using simple cylindrical Langmuir probe theory.[15] Since the Langmuir probe was swept at 10 Hz for 1 second, 20 ramps were present in each data file. These data were averaged then smoothed using a Savitzky-Golay filter.[16,17] Then, the derivative of the probe current with respect to the probe voltage was plotted against the probe voltage. The voltage corresponding to the highest amplitude value on this plot is roughly equal to the plasma potential. This potential is needed to correct the RPA reading because the RPA ion retarding grid was biased with respect to the facility ground. The true filter voltage was equal to the ion retarding grid bias voltage minus the local plasma potential.

B. RPA Analysis

RPA analysis was carried out by first smoothing the RPA trace then taking the negative of the derivative of the collector current with respect to the bias voltage on the ion retarding grid. The result, plotted against the bias voltage, is proportional to the ion energy per charge distribution function.[18] Traditionally, the most probable voltage is taken as the average ion energy per charge. The most probable voltage is defined as the voltage where the amplitude of the plot maximizes. However, due to a combination of noise and broad ion distribution, the data taken for the 200 V, 49.8 A case had a small peak on top of the main population that skewed the location of the most probable voltage. To deal with this issue, the average ion energy per charge was calculated via ensemble-averaging using only the part of the trace where the amplitude exceeded half of the maximum amplitude. This averaging approach will be referred to as the threshold-based averaging approach with a 50% threshold. For clean traces, this approach yield values that are at most 3-4 V different from the most probable voltage. For noisy traces, this approach yield values that are insensitive to noise spikes. Figure 6 shows plots from applying the threshold-based averaging approach to the RPA data obtained for the 200 V, 49.8 A condition. The black dashed vertical line indicates the location of the most probable voltage, the red solid vertical line indicates the result of using the threshold-based averaging approach with the 50% threshold, and the red dashed horizontal line indicates the 50% of maximum threshold.

Note that in theory the most accurate result is obtained by ensemble-averaging the entire RPA trace. However, doing so often produces unphysical results because the ion energy per charge distribution as measured by the RPA is typically much broader than the real distribution due to the wide acceptance angle of the RPA. This is also the reason the traditional approach relies on the most probable voltage. Using the 50% threshold-based ensemble averaging essentially strikes a balance between excluding broadened data and maintaining some degree of noise insensitivity.

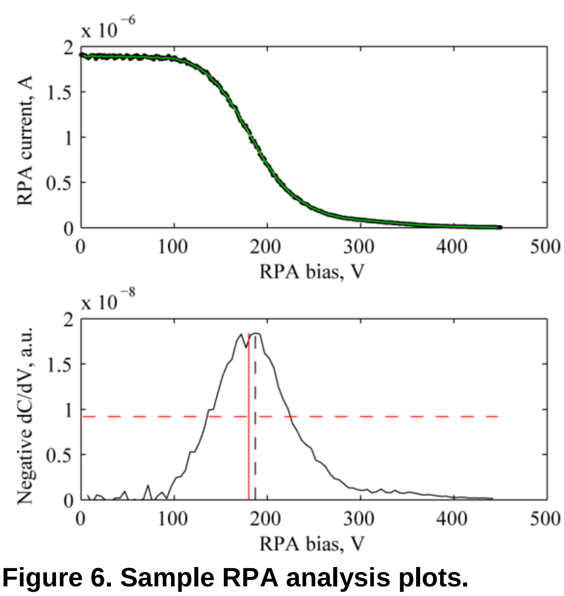

Figure 6. Sample RPA analysis plots.

The ion energy per charge obtained from the RPA, corrected by the Langmuir probe measurement, was inputted into the CEX model used in the analysis of the ExB probe data. CEX depletes lower-charge-state species more than higher-charge-state species, so the effect of ion CEX collisions with facility background neutrals must be accounted for. This effect is especially prominent for high-power thruster tests. One can approximate the ion energy per charge as the discharge voltage. Doing so removes the dependence of the ExB probe analysis on the RPA and Langmuir probe data, though with a small increase in uncertainty. See Shastry's work for an estimate of this uncertainty.[9]

C. Traditional Approaches for ExB Probe Analysis

The ExB probe is strictly a velocity filter. Since different charged species are accelerated to different velocities by going through roughly the same potential drop, they will show up as different peaks when interrogated by the ExB probe. Traditionally, the simplest ExB probe analysis approach is to take the height of each peak and assume they are proportional to the current of the respective species. This approach is identical to assuming mono-energetic particles for each species.[19,20] The peak height approach is also used as a last resort if the width of the ion velocity distribution measured by the ExB probe is around the same or less than the ExB probe's velocity resolution. In such a case, the large ExB probe velocity resolution causes artificial broadening of the recorded traces.

If the ExB probe velocity resolution is at least several times smaller than the width of the measured ion distribution, the preferred method for analyzing ExB probe data is by integration. Most integration schemes involve fitting some general distribution equation form to the ExB probe trace. Then, the area under the curve is calculated either by geometry or by numerical integration. Curve-fit and integration are used together because the ion distributions from different charged species tend to overlap in the regions between peaks, making integration of only one species at a time impossible without some kind of assumption on the form of the distribution. The domain of the curve-fit for each species generally need to be bounded such that only current signal generated by one species is being fitted at a time.

One of the earliest examples of the traditional integration approaches is the half-width-at-half-maximum (HWHM) triangle fit, proposed by Beal.[21] In this approach, the current due to each species is assumed to be proportional to the product of the peak height and the HWHM value. This is equivalent to fitting a triangle to the measured ExB probe trace for each species in such a way that the peak and HWHM value of the triangle match those of the species' distribution.

Another curve-fit approach is the Gaussian fit, proposed by Linnell.[22] In this approach, each peak in the ExB probe trace is fitted to a Gaussian curve within a limited curve-fit domain. The curve-fit domain is individually selected for each species so that most of the current signal inside the domain is guaranteed to come from only the associated species. The integrated area under the fitted curve is assumed to be proportional to the current fraction of the associated species.

A third curve-fit form is the variable exponent fit proposed by Kim.[23] Kim attempted to find an exponent-based equation form that best fit the ExB probe data of the SPT-100 and found that the distribution function typically lies between the Gaussian, which scales with $\exp(-u^2)$, and the Druyvesteyn, which scales with $\exp(-u^4)$, where u is the particle velocity. Since the Gaussian function describes a homogeneous fluid at thermal equilibrium and a Druyvesteyn function describes a charged population in a uniform electric field with elastic collisions against a uniform background, the rationale is that the ion distribution of the Hall thruster exhaust must lie somewhere in between. Thus, Kim derived a formula where the exponent is left as a fitting parameter. Equations for the various fitting equations will be shown in the next section. Note that Kim's work is the first published instance where the ExB probe was used to study a Hall thruster and strongly influenced all subsequent work in this area including all other cited work on ExB probe studies.

Once curve-fitting is done, current fractions can be calculated via Eq. (2),[9]

$$\Omega_j \equiv \frac{I_j}{\sum_k I_k} = \frac{n_j Z_j^{3/2}}{\sum_k n_k Z_k^{3/2}} \tag{2}$$

where Ω_j is the current fraction of the j-th species, I_j is the current of the j-th species, n_j is the density of the j-th species, and Z_j is the charge of the j-th species. For the traditional integration approaches, regardless of the form of the fitting function, the current of the j-th species is calculated from the total area under the curve found in the curve-fitting step multiplied by constants that are the same across all species. Since these constants are the same, the current fraction can be calculated simply as the ratio of the integrated probe current for a given species divided by the sum of integrated probe current. The species fraction can be calculated using Eq. (3),[9]

$$\zeta_j \equiv \frac{n_j}{\sum_k n_k} = \frac{\Omega_j / Z_j^{3/2}}{\sum_k \Omega_k / Z_k^{3/2}} \tag{3}$$

where ζ_j is the species fraction of the j-th species. Note, that the last term of Eqs. (2) and (3) only applies if one can assume negligible variation in acceleration voltage for different species. The effect of background CEX is typically corrected at this step by modifying the integrated current and integrated density. The CEX correction scheme used in this study is described in Shastry's work[9] and reproduced in Eqs. (4)-(6),

$$(J/J_0)_{Xe^{+}} = \exp(-n_0\sigma_1 z), \quad \sigma_1 = 87.3 - 13.6\log(V_1) \tag{4}$$

$$(J/J_0)_{Xe^{2+}} = \exp(-n_0\sigma_2 z), \quad \sigma_2 = 45.7 - 8.9\log(2V_2) \tag{5}$$

$$(J/J_0)_{Xe^{3+}} = \exp(-n_0\sigma_3 z), \quad \sigma_3 = 16.9 - 3.0\log(3V_3) \tag{6}$$

where J is the current density at distance z away from the thruster exit plane, J_0 is the current density at the thruster exit plane, and n_0 is the average background neutral density. The numerical formulas for the CEX cross-sections, σ_1, σ_2, and σ_3, are given in units of $Å^2$ (10^{-20} m^2). The ion energy per charge, V_1, V_2, and V_3 for Xe^{+}, Xe^{2+}, and Xe^{3+}, respectively, are assumed to be equal to the average ion energy per charge as measured by the RPA. The value of n_0 is calculated by converting the average of the pressure measurement from four ion gauges. Two of these gauges were located on the chamber wall at the same axial position as the farfield probe tower, one of the gauges was next to the thrust stand, and the last of the gauges was on the chamber wall at an axial location close to the thruster.

In summary, the typical approach is to perform a curve-fit for each peak using the VDF form of choice, integrate the current, apply the CEX correction, calculate the current fraction, and, if necessary, calculate the species fraction from the current fraction.[9] The current fraction can then be used in any of a number of phenomenological efficiency models. These models are designed to help researchers identify trends in the various physical processes that drive the overall efficiency of a Hall thruster. The phenomenological efficiency model used in this study will be described in a later section.

D. New Approach for ExB Probe Analysis

The approach used to analyze the ExB probe data for this study was derived from scratch and closely matches the derivation by Kim.[24] However, Kim did not publish the exact integration formula used to calculate the species fraction and did not try to calculate the current fraction (that was not his objective). To the best of the authors' knowledge, the integration formulas presented in this paper are original and not published in any prior work.

To figure out the relationship between the current fraction and the ExB probe trace we will first look at the physical description of what exactly the ExB probe is collecting at a given plate bias voltage. This is shown in Eqs.(7), (8), and (9),

$$I_P(V_P) = \sum_j I_{P,j}(V_P) \tag{7}$$

$$I_{P,j}(V_P) = Z_j e A_P n_j \int_{u_0-\Delta u}^{u_0+\Delta u} u f_j(u)\, du \tag{8}$$

$$u_0 = \frac{E_0}{B_0} = \frac{V_P}{B_0 D_f} \tag{9}$$

where I_P is ExB probe collector current, V_P is the plate bias voltage, $I_{P,j}$ is the contribution to the measured current by the j-th species, e is the elementary charge, A_P is the probe entrance area, u is particle velocity, u_0 is the particle velocity corresponding to the applied electric and magnetic field magnitude, E_0 and B_0, respectively, as shown in Eq. (9), Δu_j is the half-width of the ExB velocity resolution (its charge dependence is derived in the appendix), f_j is the velocity distribution function (VDF) of the j-th species, and D_f is the gap between the ExB bias plates.

For an ExB probe with good velocity resolution, that is to say $\Delta u_j << u_0$, the integral term can be approximated as $f_j(u_0)*2\Delta u_j$. The derivation of the dependence of Δu_j on other basic parameters is shown in the appendix. The final result is replicated in Eq. (10) for convenience,

$$\Delta u_j = \frac{m u_0^2}{Z_j e B_0} G \tag{10}$$

where m is the mass of the particle and G is a function of only geometric constants. Taking the $\Delta u_j << u_0$ approximation and substituting Eq. (10) into Eq. (8), we arrive at Eq. (11),

$$I_{P,j}(V_P) = K_0 u_0^3 n_j f_j(u_0), \quad K_0 \equiv \frac{2 A_P m G}{B_0} \tag{11}$$

where K_0 is a constant for a given probe design and propellant atomic mass. Further substituting Eq. (9) into Eq. (11), we arrive at Eq. (12),

$$I_{P,j}(V_P) = K_1 n_j V_P^3 f_j(K_2 V_P), \quad K_1 \equiv \frac{K_0}{(B_0 D_f)^3}, \quad K_2 = \frac{1}{B_0 D_f} \tag{12}$$

where K_1 and K_2 are constants for a given probe design. Depending on which VDF form is in use, the associated equation is substituted into f_j, and Eq. (12) is fitted to the ExB probe trace to solve for any fitting constant. The formulas presented so far, though appearing in different forms, matches previously published work.[9,23] The formulas to follow are original and diverge from past work.

To calculate the species fraction and current fraction, we now need the integral equations relating each quantity to the ExB probe current. To find the species fraction, we begin by re-arranging the V_P^3 term, then integrating both sides of Eq. (12) with respect to V_P from 0 to ∞. Since n_j does not depend on V_P it can go outside the integral. The result is shown in Eq. (13). Since the integral of f_j from 0 to ∞ is unity, we can further simplify the result, which is shown in Eq. (14).

$$K_1 n_j \int_0^\infty f_j(K_2 V_P)\, dV_P = \int_0^\infty \frac{I_{P,j}(V_P)}{V_P^3} dV_P \tag{13}$$

$$n_j = \frac{1}{K_1} \int_0^\infty \frac{I_{P,j}(V_P)}{V_P^3} dV_P \tag{14}$$

Equation (14) relates n_j to the ExB probe current and can be used to calculate the species fraction. The integration formula for species fraction is shown in Eq. (15).

$$\zeta_j \equiv \frac{n_j}{\sum_k n_k} = \frac{\int_0^\infty \frac{I_{P,j}(V_P)}{V_P^3} dV_P}{\sum_k \int_0^\infty \frac{I_{P,k}(V_P)}{V_P^3} dV_P} \tag{15}$$

To find the current fraction, we begin by relating the current of the j-th species, I_j, to the ExB probe current. The current of the j-th species is defined in Eq. (16). Substituting Eq. (9) into (16) yields Eq. (17).

$$I_j = Z_j e A_P n_j \int_0^\infty u_0 \, f_j(u_0)\, du_0 \tag{16}$$

$$I_j = Z_j e A_P K_2^2 n_j \int_0^\infty V_P \, f_j(K_2 V_P)\, dV_P \tag{17}$$

Next, we rearrange Eq. (12) by dividing both sides by V_P, then integrate both sides with respect to V_P from 0 to ∞ to obtain Eq. (18). Substituting Eq. (18) into Eq. (17) yields Eq. (19).

$$n_j \int_0^\infty V_P \, f_j(K_2 V_P)\, dV_P = \frac{1}{K_1} \int_0^\infty \frac{I_{P,j}(V_P)}{V_P^2} dV_P \tag{18}$$

$$I_j = \frac{Z_j e A_P K_2^2}{K_1} \int_0^\infty \frac{I_{P,j}(V_P)}{V_P^2} dV_P \tag{19}$$

Equation (19) relates I_j to the ExB probe current and can be used to calculate the current fraction. The integration formula for the current fraction is shown in Eq. (20).

$$\Omega_j \equiv \frac{I_j}{\sum_k I_k} = \frac{Z_j \int_0^\infty \frac{I_{P,j}(V_P)}{V_P^2} dV_P}{\sum_k Z_k \int_0^\infty \frac{I_{P,k}(V_P)}{V_P^2} dV_P} \tag{20}$$

In the new ExB probe analysis approach, the process starts with selecting a form for the VDF, then inserting the form into Eq. (12) and performing a curve-fit to the ExB probe current as a function of bias plate voltage for each species. Using the result, Eq. (15) and (20) are then numerically integrated to obtain the species fraction and current fraction, respectively. The CEX correction is applied prior to normalization. For all ExB probe analysis carried out in this study, the curve-fit process starts by curve-fitting the highest charge peak present (Xe^{4+}), subtracting it out from the probe trace, then proceeding to lower charge peaks. Xe^{4+} data is not used in the final current and species fraction calculation because it typically comprises less than 0.5% of the beam current. However, Xe^{4+} curve-fit is still performed and result subtracted to make curve-fitting of lower charge states easier.

Listed in Eqs. (21)-(24) below are the forms of several VDFs that were tried in the current study. They are, in order, triangle, Gaussian, variable exponent, and twin Gaussian.

$$\text{Triangle:} \quad f_j(u) = \begin{cases} (-a/b) * |u-c| + a, & c-b < u < c+b \\ 0, & \text{else} \end{cases} \tag{21}$$

$$\text{Gaussian:} \quad f_j(u) = a * \exp[-b(u-c)^2] \tag{22}$$

$$\text{Variable Exponent:} \quad f_j(u) = a * \exp[-b|u-c|^n] \tag{23}$$

$$\text{Twin Gaussian:} \quad f_j(u) = a_1 * \exp[-b_1(u-c_1)^2] + a_2 * \exp[-b_2(u-c_2)^2] \tag{24}$$

where a, b, c, n, a_1, b_1, c_1, a_2, b_2, c_2, are fitting constants. Note the triangle form listed here is not quite equivalent to the HWHM triangle method described earlier because this VDF will actually be fitted to the ExB probe data as opposed to having only its peak and width matched. The triangle form is tried because it is a close match to the HWHM triangle method and because the HWHM triangle method is incompatible with the new integration formulas. The twin Gaussian form was tried in an attempt to capture the tail that is often observed in the VDFs of accelerated ions in a Hall thruster. While this form generally gives a much better fit to the data than any other form, it can generate an erroneous result if the curve-fit boundary is not properly chosen. For instance, if the boundary includes peaks from two different species, the computer will fit the twin Gaussian form to both peaks and treat them as a single species. The operator must study each curve-fit plot to ensure this is not occurring during data analysis.

As a side note, the traditional integration formula for the current fraction can be written as Eq. (25).

$$\Omega_j \equiv \frac{I_j}{\sum_k I_k} \approx \frac{\int_0^\infty I_{P,j}(V_P)\,dV_P}{\sum_k \int_0^\infty I_{P,k}(V_P)\,dV_P} \tag{25}$$

While Eq. (25) is mathematically incorrect, it turns out to be a pretty good approximation of Eq. (20) for analyzing the plume of a Hall thruster, especially when the VDF is narrow. A comparison between the traditional and the new integration formulas will be made in the results section.

E. Faraday Probe Analysis

Faraday probe data are used to calculate the plume divergence angle and the total ion beam current. The cosine of the momentum-weighted plume divergence angle is defined as the average axial velocity of the particles divided by the average velocity of the particles. However, momentum-weighted divergence angle is difficult to measure. The typical approach is to measure the charge-weighted divergence angle, which is approximately equal to the momentum-weighted divergence angle if the current fraction is roughly constant across the interrogated domain. For a polarly-swept probe, Eq. (26) can be used to calculate the charge-weighted divergence angle,

$$< \cos\delta > = \frac{2\pi R_{FP}^2 \int_0^{\pi/2} j(\theta)\,\cos\theta\,\sin\theta\,d\theta}{2\pi R_{FP}^2 \int_0^{\pi/2} j(\theta)\,\sin\theta\,d\theta} \tag{26}$$

where δ is the charged-weighted divergence angle, θ is the polar angle and is equal to 0° for particles traveling parallel to the firing axis, and j(θ) is the ion current density as a function of the polar angle. R_{FP} is the distance from the Faraday probe collector to the thruster center at exit plane and is constant for a polar sweep. Note the denominator is equal to the total ion beam current.

For a nude Faraday probe with a guard ring like the one used in this study, the effective collector area is not exactly equal to the collector frontal surface area. Current that enters the gap between the collector and the guard ring can be collected by the side surfaces of the collector.[25] According to work by Brown, the current entering the gap is collected by the collector and the guard ring in ratio proportional to the ratio of exposed gap area.[25] For the probe design used in the current study, the area inside the gap is dominated by area connected to the guard ring (See Fig. 5). However, there is enough area connected to the collector that some level of correction is needed. Note that only the part of the gap with direct exposure to the incoming ion beam is used in the gap area calculation. Using the approach recommended by Brown, the effective collection area is ~4% greater than the collector frontal area. The effective collection area is used for all Faraday probe analysis.

Much like in the analysis of the ExB probe data, CEX is a factor in Faraday probe data analysis. However, whereas CEX is an attenuating factor for ExB probe data, it is a re-distributing factor for Faraday probe data. This is because CEX ions have a different trajectory than the ion it is born from and will tend to show up in the wings of a Faraday probe trace. The region considered the “wings” of a Faraday probe trace can be seen in Fig. 7 as the region outside of the two outermost dashed vertical lines. An ExB probe does not see CEX ions because of a combination of small acceptance angle and a tendency to de-emphasize low speed ions. The ExB filter resolution has a dependence on the square of the particle speed and CEX ions have only a small fraction of the speed of beam ions. The best way to correct for the re-distributing behavior of CEX on Faraday probe traces is to take data at multiple distances and facility background pressures.[25] This could not be carried out for the current study due to time constraints. Instead, an extrapolated-wing approach is used to remove the parts of the trace that are believed to be dominated by re-distributed CEX ions. The extrapolated-wing approach begins by plotting the ion current density on a semi-log scale. Curve-fits are then performed on the data from a polar angle of 10° to 25°. The curve-fit result is then extrapolated to 90°. Figure 7 shows a graphical representation of the extrapolated-wing method. The black solid line is the raw data. The dashed vertical line in the middle is the center of the trace (θ is not quite equal to 0° here due to a minor mis-alignment in the physical setup). The left two and right two dashed vertical lines indicate the boundary for the data used to perform the curve-fit on the respective side. The light green solid lines represent the curve-fit results.

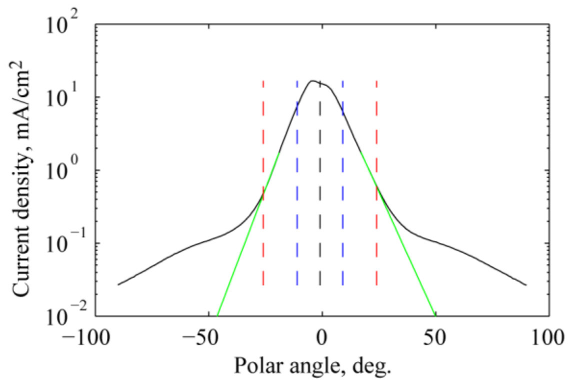

Figure 7. Illustration of the extrapolated-wing method for analyzing Faraday probe data.

In past studies, low secondary electron emission (SEE) yield materials like molybdenum and tungsten have been used for the collector.[7,26,27] Secondary electrons born on a negatively biased probe will accelerate away from the probe. This effect adds extra current to the probe measurement that is indistinguishable from the collected ion current. By selecting a low SEE yield material, researchers had believed that the effect of SEE is negligible and can be ignored. While singly-charged xenon-induced SEE yield for molybdenum and tungsten are negligible (0.013 to 0.022), the doubly-charged xenon-induced SEE yield are roughly 10 times higher than the singly-charged yield, and the triply-charged SEE yield are roughly 35 times higher than the singly-charged yield.[28-30] Furthermore, Hagstrum discovered that metastable singly-charged xenon induces roughly the same SEE yield as doubly-charged xenon.[31] Thus, as long as the plume of the thruster is composed of mostly ground-state singly-charged xenon ions, the assumption of negligible SEE effect holds.

Table 1. Summary of SEE data for xenon ion bombardment of molybdenum.[28,29]

Bombarding particle	SEE yield of molybdenum
Xe^+	0.022
Xe^{2+}	0.20
Xe^{3+}	0.70

During the present testing, the assumption of negligible SEE effect did not hold. The material used for the present study is molybdenum, which is considered a low SEE yield material. The reason SEE effects are not negligible is because high-power Hall thrusters appear to produce 20-30% doubly- plus triply-charged ions by current fraction. Combined with the high SEE yield associated with bombardment by higher charge ions, the effect on Faraday probe measurements is in the range of 5-10%. To correct for SEE effects on the Faraday probe measurement, we turn to data published by Hagstrum. Table 1 summarizes the SEE yield values used in the data analysis of the present study. The singly-charged and doubly-charged xenon-induced yields are averages of the SEE yield data for ion energies in the range of 200 to 800 eV in Hagstrum's 1956 work on molybdenum.[29] For both of these parameters, the value measured by Hagstrum varied by no more than 10% of the listed average. A published value for the triply-charged xenon-induced yield of molybdenum could not be found. The value in Table 1 is a projected value based on the similarity in yield between tungsten and molybdenum. The ratio of triply-charged induced yield to doubly-charged induced yield for tungsten is 3.5, so the yield for molybdenum is projected to be 3.5 * 0.2, or 0.7.[28] The search for a more accurate triply-charged xenon-induced SEE yield of molybdenum is left for future work.

Equation (27) shows the relationship between the actual ion current density, the various SEE yield values, and the ion current density measured by the Faraday probe.

$$J = \frac{J_{FP}}{1+\gamma_{eff}} = J_{FP} * \sum_k \frac{\Omega_k}{1+\gamma_k} \qquad (27)$$

where J is the actual ion current density, J_{FP} is the current density measured by a nude Faraday probe, γ_{eff} is the effective SEE yield, and γ_k is the SEE yield associated with bombardment by the k-th species.

Using Eq. (27), we can write a new equation to show the definition of the effective SEE yield for the Faraday probe, shown in Eq. (28).

$$\gamma_{eff} = \frac{1}{\left(\sum_k \frac{\Omega_k}{1+\gamma_k}\right)} - 1 \tag{28}$$

For the present study, the effective SEE yield range from 0.06 to 0.09, which is not a negligible amount. The amount of metastable singly-charged ions is assumed to be negligible. This assumption is an extrapolation from controlled ion beam work done by Hagstrum.[31] In his experiment, Hagstrum varied the energy of the electrons used to generate his singly-charged ion beam from 10 to 70 eV. The SEE yield he measured jumped quickly up from 0.022 to 0.025 when the electron energy was ramped up from 25 to 30 eV, and then plateaued out at 0.025 all the way up to 70 eV. While the Hall thruster ionization zone and an ion beam discharge chamber are not exactly the same they do share many of the same operating principles, including a reliance on impact bombardment ionization. Since the amount of metastable ions was so small that the SEE yield increased by only 0.003 for Hagstrum's experiment, we assumed the effect will be of similar magnitude in a Hall thruster and is therefore negligible.

F. Phenomenological Efficiency Model

A phenomenological efficiency model is a way of breaking down and describing various physical phenomena that affect the overall efficiency of a thruster. The purpose of a phenomenological efficiency model is to help researchers identify trends in the processes that drive the overall thruster efficiency. Many efficiency models have been proposed for the Hall thruster in the past. The complexity of these models depended on the operating environment and the state of knowledge in the community at the time. The model used in this paper is the same as a prior work by Shastry,[9] which has evolved over time from a number other studies.[8,14,24,32] It is shown in Eq. (29) to (34).

$$\eta_a = \eta_v \eta_d \eta_b \eta_m \eta_q \tag{29}$$

$$\eta_v = \frac{V_{RPA}}{V_d} \tag{30}$$

$$\eta_d = (\cos\delta)^2 \tag{31}$$

$$\eta_b = \frac{I_b}{I_d} \tag{32}$$

$$\eta_m = \left(\frac{m_{Xe} I_b}{\dot{m}_a e}\right)\alpha_m, \quad \alpha_m = \sum_k \frac{\Omega_k}{Z_k} \tag{33}$$

$$\eta_q = \frac{\left(\sum_k \Omega_k / \sqrt{Z_k}\right)^2}{\sum_k \Omega_k / Z_k} \tag{34}$$

where η_a is the anode efficiency, which can also be calculated via Eq. (1), η_v is the voltage utilization efficiency, η_d is the divergence efficiency, η_b is current utilization efficiency, η_m is the mass utilization efficiency, η_q is the charge utilization efficiency, V_{RPA} is the ion energy per charge measured by the RPA, I_b is the total beam current measured by the Faraday probe, m_{Xe} is the mass of xenon, and α_m is the part of mass utilization efficiency that is calculated from ExB probe data. The voltage utilization efficiency describes, on the average, how much of the voltage drop provided by the discharge supply is actually used to accelerate the ions. The divergence efficiency describes how much of the kinetic energy imparted to the ions is axial, thrust-producing, kinetic energy. The current utilization efficiency describes how much of the discharge current is carried by ions instead of electrons. Electrons generate negligible thrust compared to the ions. The mass utilization efficiency describes how much of the mass flow exiting the thruster channel is in the form of ions. The charge utilization efficiency is a number of terms representing the effects of having multiply-charged species that are not already described by the other terms.

G. Uncertainty Analysis

Due to time constraints, a full uncertainty analysis will not be carried out for every element of this study. Only uncertainties associated with novel parts of the study and uncertainties that are dominant will be analyzed. The uncertainty in the anode efficiency as calculated by Eq. (1) from the measured thrust is dominated by the uncertainty in the thrust and is ~4% when calculated via standard error propagation.

The uncertainty in the voltage utilization as calculated from Eq. (30) is ~1%. This uncertainty is a combination of the uncertainty in the RPA analysis method and the Langmuir probe analysis method used to correct the RPA measurement. The uncertainty in the charge utilization as calculated from Eq. (34) is expected to be less than 0.5%. That is because this value is very insensitive to the value of the current fraction. For the current study, the charge utilization value varied from 0.974 to 0.98.

The uncertainty in the divergence efficiency, current utilization efficiency, and mass utilization efficiency varies greatly from condition to condition. Specifically, the ExB probe trace for the 200 V, 50 A, 300 V 50 A, and 300 V, 67 A cases are highly abnormal. The abnormality will be shown and discussed in the results section. With the exception of these three cases, the uncertainties of the aforementioned three efficiencies are as follows.

For the divergence efficiency, the important sources of uncertainty include background CEX effects and SEE effects. Based on prior work by Brown, Faraday probe data taken at 5 MTD away from the thruster should have an uncertainty of no more than 2% for the facility background pressure found during the current study.[25] However, Brown's work was done on a lower power thruster (nominal 6 kW) compared to the 300M (20 kW) and with a correspondingly shorter distance between the probe and the thruster. The uncertainty associated with CEX is estimated to be ~3% based on the extra distance between the probe and thruster. The effect of SEE on the uncertainty of the divergence efficiency is more difficult to calculate due to lack of prior experience. However, as long as the current fraction only undergoes small changes as a function of polar angle, the overall error will be small. This is because SEE represents a relatively small correction to the local current density. Small changes to a small correction should be negligible. Thus, the overall uncertainty in the divergence efficiency is estimated to be 3%.

Before continuing on to the current utilization, the uncertainties associated with the ExB probe will be examined. Based on the equations derived in the appendix, the average velocity resolution of the ExB probe is 2.7%. This value is higher for ions with higher energy per charge and is no more than 3.5% for the detectable ion populations with the highest energy per charge. This resolution is sufficiently fine so that the previously mentioned ExB probe analysis methods are applicable. The ExB probe resolution primarily affects broadening of the measured VDF and has minimal effect on the current fractions. The uncertainty in the current fraction is expected to be dominated by uncertainty in the average background neutral density measured by the ion gauges. The ion gauges are nominally 6% accurate. However, they only measure the neutral density in the immediate vicinity. Factors like conductance losses and un-compensated temperature effects on the electronics are expected to raise the uncertainty of the neutral density measurement to ~15%. Substituting in a ±15% neutral density uncertainty into the CEX correction formula yields average uncertainties of ±0.035, ±0.023, and ±0.013 for the Xe^{+}, Xe^{2+}, and Xe^{3+} current fractions, respectively.

The uncertainty in the current utilization is primarily influenced by uncertainties associated with calculation of the effective collector area, CEX effects, and SEE effects. The effective collector area is expected to be accurate to ~1% based on different ways in which the gap current can be distributed between the collector and the guard ring. The use of the extrapolated-wing approach should remove much of the uncertainty associated with the CEX effect, but without additional knowledge about how much uncertainty is removed, the same 3% that was used in the calculation of the uncertainty of the divergence efficiency will be used here. The uncertainty in the SEE correction depends on the uncertainty of the current fractions calculated from the ExB probe data. Substituing in uncertainties in the current fractions calculated above into the SEE correction equation (Eq. (27)) the uncertainty in the SEE yield is

±0.014. Thus the uncertainty in the current utilization due to SEE correction is ~1.4%. The total uncertainty in the current utilization, calculated from standard error propagation, is ~3.5%.

The uncertainty in the mass utilization is dominated by the uncertainty in the measured anode mass flow rate, the total beam current, and the current fraction-dependent factor, α_m. The mass flow rate measurement has an instrumentation uncertainty of ~1%. The uncertainty in the total beam current is the same as the uncertainty in the current utilization (~3.5%). The uncertainty in α_m, which is calculated from the current fractions, is dominated by uncertainty in the average background pressure. Using ±15% neutral density and carrying through the calculations for α_m yield an average uncertainty of ~2%. The total uncertainty, calculated from standard error propagation, in the mass utilization is ~4%.

Using standard error propagation, the total uncertainty in η_a calculated via Eq. (29) for operating conditions other than 200 V, 50 A, 300 V 50 A, and 300 V, 67 A is ~6%. As previously mentioned the ExB probe data for those three operating conditions were abnormal and will be discussed separately. All calculations made in this section assume the sources of error are random in nature.

IV. RESULTS

A. ExB probe results and comparison between various ExB probe analysis methods

For the ExB probe analysis in this paper, the new integration approach with the twin Gaussian form is assumed to be the most accurate approach, and the associated results will be referred to as the baseline results. Results from applying both the new and old (traditional) integration approaches with various VDF forms, as well as with the simple peak approach, will be compared to the new integration approach with twin Gaussian form. For all ExB probe analysis methods, the analysis program begins by finding the location of the four peaks representing the first four charged states. For each charged state the left integration boundary is set to one third the distance from the peak being analyzed to the adjacent peak; the right integration boundary is set to 1.5 times the peak location. Several sample plots of how the ExB probe analysis program functions will be examined next.

Figure 8 shows a set of analysis plots generated by the program that performs ExB probe analysis. The analysis method used is the new integration approach with twin Gaussian form. The operating condition is 500 V, 40 A. For convenience, the paper will refer to the six subplots in order from left to right, top to bottom as (a) to (f). Subplot (a) shows the raw ExB probe data as black data points with red dashed vertical lines showing the location of the first four peaks. Subplots (b), (c), (e), and (f) show the four steps in the curve-fitting process. The curve-fitting process fits the appropriate form equation to the 4th peak, subtracts the fitted data from the raw trace, then fits the 3rd peak, and so on. The data prior

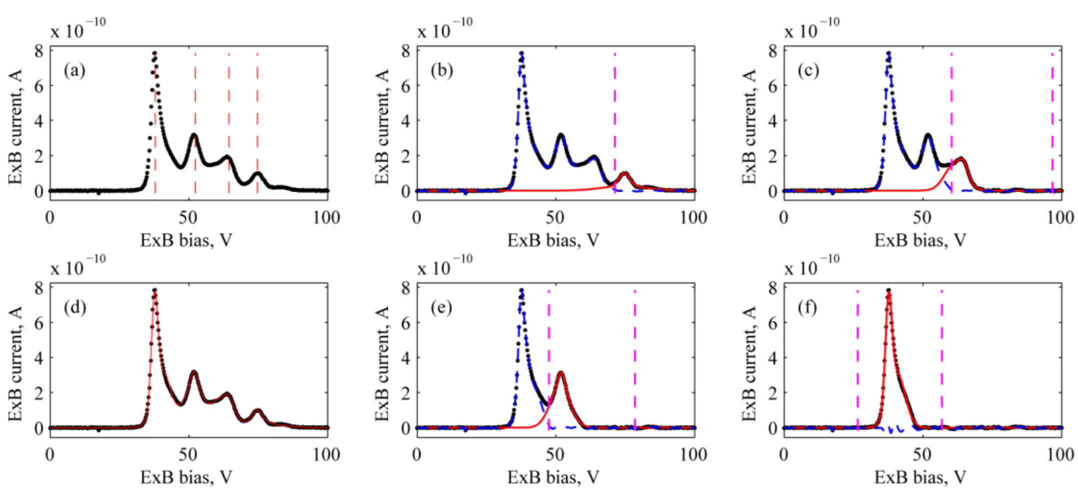

Figure 8. ExB probe analysis plots for the new integration approach with twin Gaussian form. *The 300M was operating at 500 V, 40 A.*

to the fit at each curve-fit step is shown in black dots, the red solid line shows the curve-fit, the magenta dashed vertical lines show the curve-fit boundaries, and the blue dashed line shows the leftover result after subtraction. Subplot (d) shows the raw data in black dots with a red solid line that represents the sum of all four curve-fit steps superimposed on top. Figures 9 to 11 show similar plots for the ExB probe analysis using the new integration approach with the triangle form, Gaussian form, and variable exponent form, respectively. The operating condition is 500 V, 40 A for these three figures.

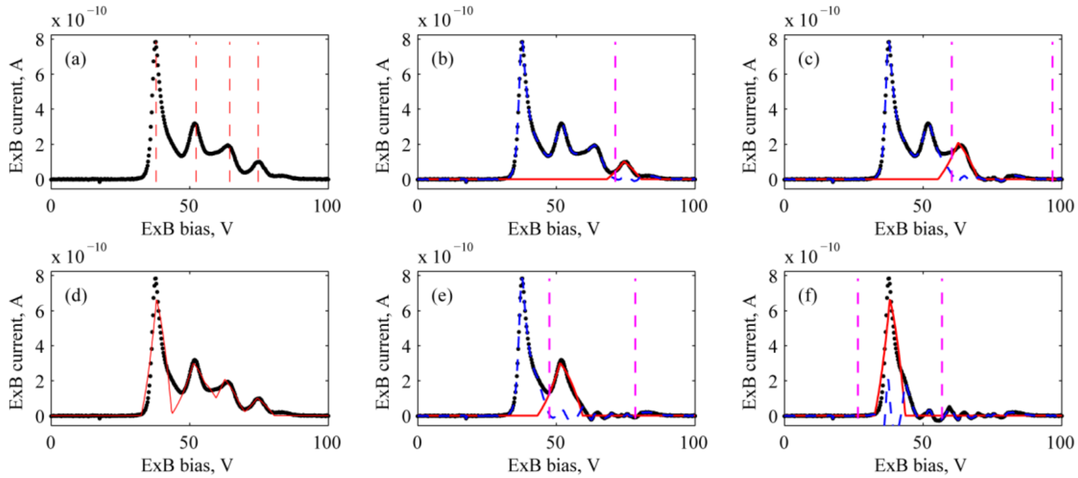

Figure 9. ExB probe analysis plots for the new integration approach with triangle form.
The 300M was operating at 500 V, 40 A.

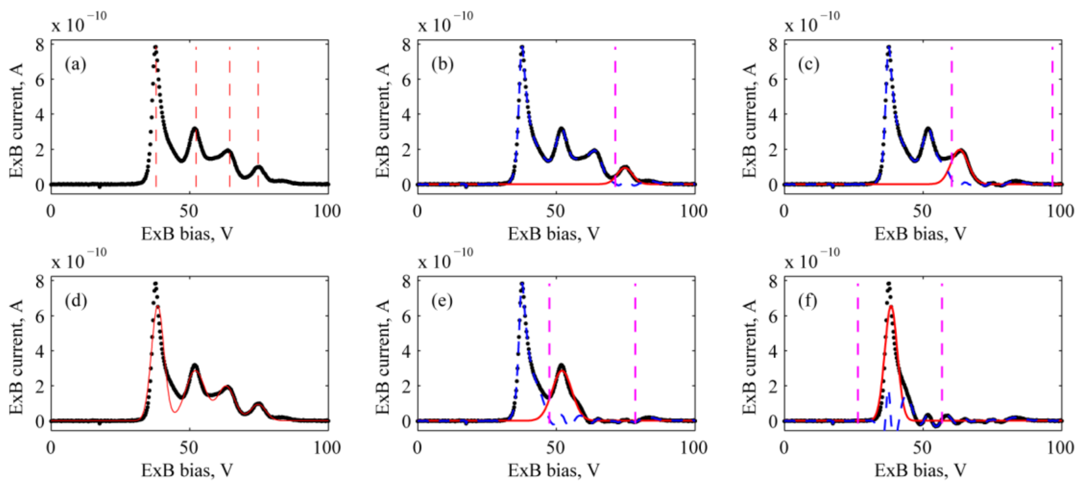

Figure 10. ExB probe analysis plots for the new integration approach with Gaussian form.
The 300M was operating at 500 V, 40 A.

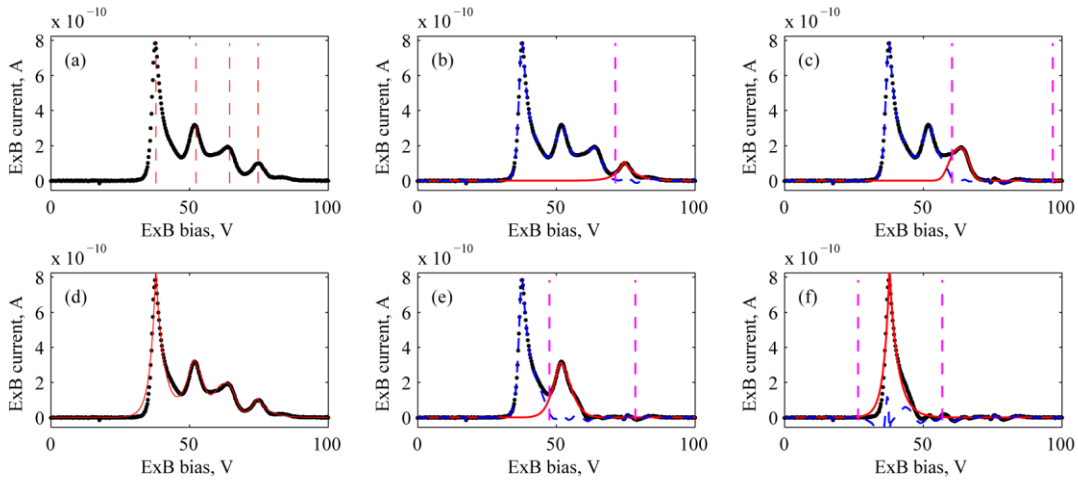

Figure 11. ExB probe analysis plots for the new integration approach with variable exponent form. *The 300M was operating at 500 V, 40 A.*

By comparing subplot (d) of Figs. 8 to 11, the twin Gaussian form appears to provide the best fit to the ExB probe data. The variable exponent form also provides a very good fit to the data. Note that a good fit to the data does not necessarily imply accurate results, though a bad fit to the data makes the analysis results questionable. Having established that the ExB probe analysis program is performing the curve-fits correctly, the results from using various analysis methods will now be compared. The parameter used for this comparison is α_m. This parameter is known to vary the greatest of all the terms in the phenomenological model used in the current study.[9] For comparison, data from conditions other than 200 V, 50 A, 300 V, 50 A, and 300 V, 67 A will be used. Those three conditions will be treated separately later. The parameter α_m is calculated for each method and for each of the seven operating conditions. The calculated values are then subtracted by the baseline value and the differences are divided by the baseline value to obtain relative percent differences. Both the average and the standard deviation of this relative difference are listed in Table 2. If the average is close to 0, the method in question yields results that are generally the same as the baseline. If the standard deviation is close to 0, the method in question yields results that closely match the case-by-case variation in the baseline. Thus, for a method to truly match the baseline, both the average and the standard deviation of the difference should be close to 0.

Table 2. Comparison of the relative difference in the α_m parameter for various ExB probe analysis methods.

Integration approach	VDF form	Corrected for CEX	Average relative difference	Standard deviation of relative difference
New	Twin Gaussian	Yes	Baseline	-
New	Triangle	Yes	-0.26%	0.64%
New	Gaussian	Yes	-0.51%	0.60%
New	Variable exponent	Yes	1.27%	0.57%
Old	Twin Gaussian	Yes	1.80%	0.50%
Old	Triangle	Yes	0.38%	0.71%
Old	Gaussian	Yes	0.52%	0.72%
Old	Variable exponent	Yes	1.21%	0.77%
-	Peak height	Yes	5.66%	0.92%
New	Twin Gaussian	No	-17.0%	4.5%
-	Peak height	No	-7.1%	4.7%

A number of interesting observations can be made from the results shown in Table 2. First, the difference between using the triangle, Gaussian, variable exponent, and the twin Gaussian forms is very small. Given the uncertainty in the probe data, there is no meaningful difference in α_m for the different VDF forms used. Recall the α_m parameter involves dividing current associated with higher charged states by charge. Mathematically, this division has the effect of cutting down the variation in α_m due to variation in the current fraction of higher charge states. The low sensitivity of the α_m parameter to current fraction is likely a contributing factor to the lack of meaningful differences in the choice of VDF forms. Another possible explanation for the small variation is that the exact equation form is not very important as long as the height and width of the distribution is properly captured. This explanation is supported by the fact that the triangle form gives the closest match to the baseline as the triangle form is only supposed to match the rough height and width of the particle distribution.

Second, the difference between the new and old integration approach is also small though it is systematic in nature. The old integration approach gives roughly 1% higher α_m than the new integration approach. Assuming the new integration approach is the more accurate approach, the old integration approach overestimates the charged species term in the mass utilization by ~1%. The standard deviations in the error for all methods are also fairly small, which indicate that the various methods follow the same trend as the baseline. The only method that deviates by a meaningful amount from the baseline is the peak height approach, which overestimates α_m by 5-6%. This supports the notion that the most important aspect of ExB probe analysis is to properly capture the height and width of each peak.

Third, there is a large difference when CEX is not accounted for. This result highlights the importance of CEX correction for high-power Hall thruster tests where the amount of neutrals between the probe and the thruster can be quite large.

The small difference between the new and old integration approach may seem surprising at first given the differences in the form of the integration equations in Eq. (20) and (25). The reason for the similarity lies in the fundamental scaling of these two integral equations. A quick analysis of this scaling using the ion current fraction integral will now be performed. The current fraction calculated from the old (traditional) approach will be labeled with Ω_j^O and the current fraction calculated from the new approach will be labeled with Ω_j^N. Assuming the incoming ion beam is composed of species with very narrow VDFs and all charged species undergo the same voltage drop, Eq. (20) can be simplified as shown in Eq. (35), and Eq. (25) can be simplified as shown in Eq. (36).

$$\Omega_j^N = \frac{Z_j \int_0^\infty \frac{I_{P,j}(V_P)}{V_P^2} dV_P}{\sum_k Z_k \int_0^\infty \frac{I_{P,k}(V_P)}{V_P^2} dV_P} \xrightarrow[\text{VDF}]{\text{Narrow}} \frac{Z_j n_j \bar{u}_j}{\sum_k Z_k n_k \bar{u}_k} \xrightarrow[V_d]{\text{Same}} \frac{n_j Z_j^{3/2}}{\sum_k n_k Z_k^{3/2}} \tag{35}$$

$$\Omega_j^O \approx \frac{\int_0^\infty I_{P,j}(V_P) dV_P}{\sum_k \int_0^\infty I_{P,k}(V_P) dV_P} \xrightarrow[\text{VDF}]{\text{Narrow}} \frac{n_j \bar{u}_j^3}{\sum_k n_k \bar{u}_k^3} \xrightarrow[V_d]{\text{Same}} \frac{n_j Z_j^{3/2}}{\sum_k n_k Z_k^{3/2}} \tag{36}$$

The simplified expressions for the two integration approaches are equal. The voltage drop is typically very similar between the charged species, thus for plumes with very narrow VDFs, the two approaches yield the same answer. Additionally, Eqs. (35) and (36) imply that any difference in the results between the new and old approaches arise mostly from differences in the way the two approaches account for the spread in the VDF.

As previously mentioned, the ExB probe traces for the three low-voltage, high-current conditions appear abnormal. Figures 12 to 14 show the raw ExB probe traces for the 200 V, 50 A, 300 V, 50 A, and 300 V, 67 A operating conditions, respectively. Also shown in the figures are red dashed vertical lines that indicate the approximate location where various charged species peaks should have appeared in the trace. These three traces exhibit strange characteristics where peaks do not always appear where they should have and higher-charged state peaks tend to be eclipsed by their neighbors. Analysis was carried out on these traces using the new integration approach with twin Gaussian form. However, the uncertainty is expected to be particularly large.

Table 3 summarizes the ExB probe analysis results. These results use the new integration approach with twin Gaussian form and are corrected for CEX effects. The results shown in the table confirm the original assessment that for the current data set, the values of the parameters derived from ExB probe data are largely insensitive to variations in the current fractions. However, this observation comes with the caveat that the ExB probe traces for low voltage, high current conditions appear abnormal and have high uncertainties. Conditions with abnormal ExB traces are highlighted with asterisks under the discharge voltage column.

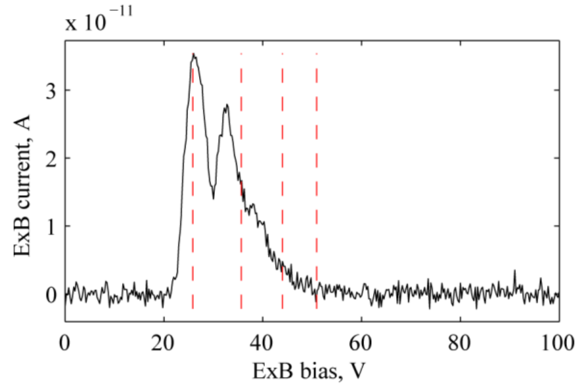

Figure 12. Raw ExB probe trace for the 200 V, 50 A operating condition.

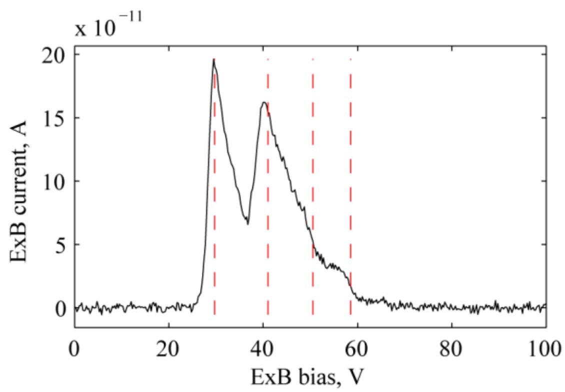

Figure 13. Raw ExB probe trace for the 300 V, 50 A operating condition.

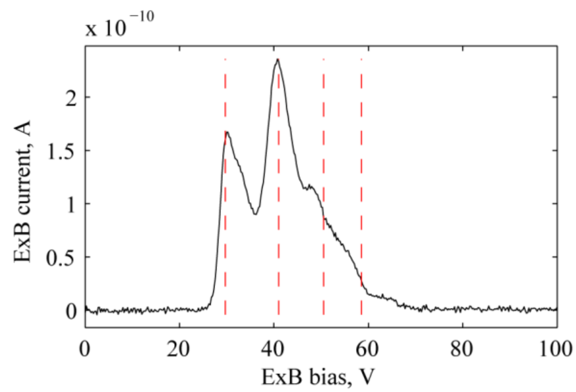

Figure 14. Raw ExB probe trace for the 300 V, 67 A operating condition.

Table 3. Summary of ExB probe data analysis results.

Asterisks in the discharge voltage column indicate conditions with abnormal ExB traces.

Discharge voltage, V	Discharge current, A	Ω, Xe^{+}	Ω, Xe^{2+}	Ω, Xe^{3+}	Species fraction, Xe^{+}	Species fraction, Xe^{2+}	Species fraction, Xe^{3+}	η_q	α_m
*200.6	49.8	0.758	0.224	0.019	0.893	0.103	0.005	0.980	0.876
300.2	33.5	0.812	0.130	0.058	0.931	0.055	0.014	0.980	0.896
*300.4	50.5	0.714	0.220	0.066	0.879	0.104	0.017	0.974	0.846
*301.3	67.8	0.738	0.200	0.062	0.890	0.094	0.016	0.975	0.859
400.1	25.4	0.788	0.140	0.072	0.921	0.062	0.018	0.978	0.882
400.7	37.5	0.776	0.139	0.085	0.916	0.062	0.021	0.976	0.874
400.6	49.8	0.785	0.140	0.075	0.919	0.062	0.019	0.977	0.880
500.3	20.2	0.752	0.177	0.071	0.901	0.082	0.018	0.976	0.864
500.7	30.2	0.793	0.145	0.062	0.921	0.064	0.015	0.979	0.886
500.4	40.3	0.759	0.163	0.078	0.906	0.074	0.020	0.975	0.867

B. Faraday probe results

Review of the Faraday probe results will start with data plots from a few cases. Figures 15 to 18 show these results. As before, the dashed vertical line in the middle of the plot is the center of the trace. The left two and right two dashed vertical lines indicate the data used to perform the curve-fit on the respective side. The light green solid lines represent the curve-fit results.

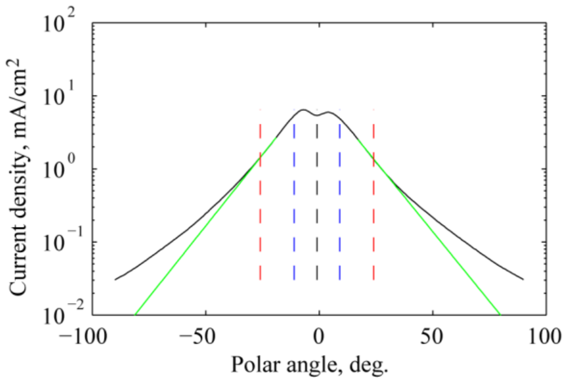

Figure 15. Faraday probe analysis plot, 200 V, 50 A.

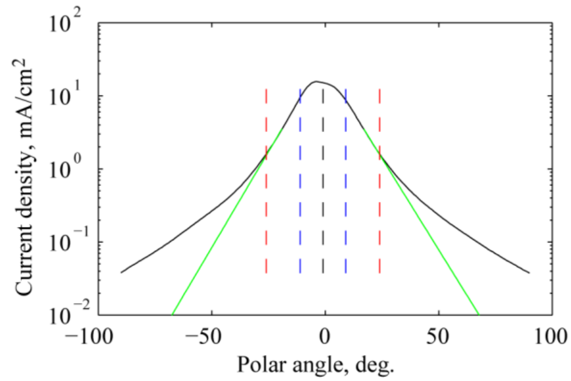

Figure 16. Faraday probe analysis plot, 300 V, 67 A.

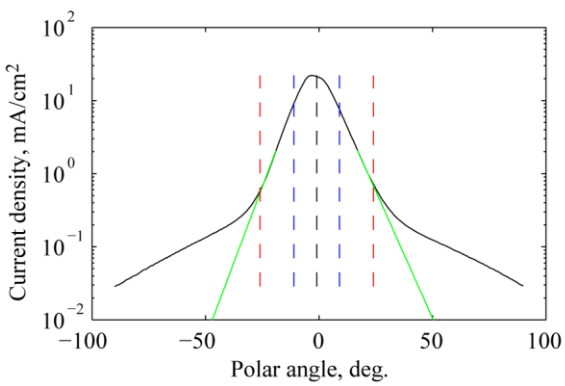

Figure 17. Faraday probe analysis plot, 400 V, 50 A.

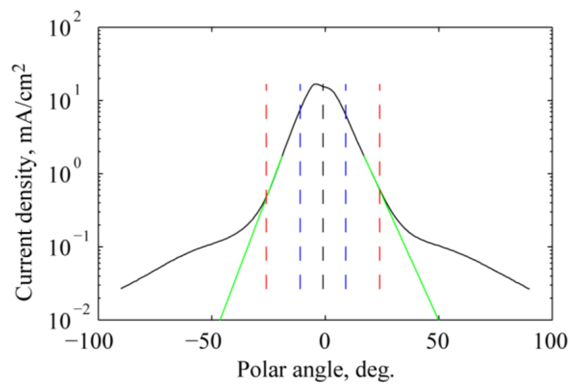

Figure 18. Faraday probe analysis plot, 500 V, 40 A.

Generally, the central portion of the Faraday probe trace tends to be more of a sharp peak for higher-discharge-voltage cases. This trend indicates the plume is more collimated when the thruster is operating at higher discharge voltages.

The CEX wings appear fairly broad for all cases. Brown previously performed a study of Faraday probe traces as a function of background pressure. In that study, the CEX wings can be seen to become more prominent with rising background pressure.[25] Although the current study was performed with a background pressure that is typically considered low in Hall thruster testing, the Faraday probe data shows that the extra distance required for interrogating higher power Hall thruster gave rise to prominent CEX wings. Recall that the minimum distance between the Faraday probe and the thruster is limited by the need to approximate the source of the plume as a point source. In future high-power Hall thruster tests, Faraday probe sweeps at multiple distances may be necessary to obtain accurate data.

Table 4. Summary of Faraday probe data analysis results.
Asterisks in the discharge voltage column indicate conditions with abnormal ExB traces.

Disch. voltage, V	Disch. current, A	Original Div. angle, deg.	Original Beam current, A	Ex.-wing Div. angle, deg.	Ex.-wing Beam current, A	Effective SEE yield	Beam current, corrected for SEE, A	η_d	η_b
*200.6	49.8	30.7	47.1	26.3	42.7	0.065	40.1	0.804	0.806
300.2	33.5	25.6	32.2	15.1	27.4	0.067	25.7	0.932	0.766
*300.4	50.5	27.0	48.9	18.4	41.6	0.086	38.3	0.901	0.759
*301.3	67.8	27.9	66.1	20.4	56.8	0.081	52.6	0.878	0.776
400.1	25.4	25.7	24.9	14.9	21.2	0.075	19.7	0.934	0.777
400.7	37.5	25.1	36.7	14.6	31.5	0.081	29.1	0.937	0.776
400.6	49.8	24.6	48.1	14.4	41.2	0.077	38.2	0.938	0.768
500.3	20.2	25.1	20.1	15.3	17.4	0.081	16.1	0.931	0.795
500.7	30.2	25.7	29.7	15.2	25.6	0.072	23.9	0.931	0.792
500.4	40.3	25.1	39.6	14.7	34.0	0.082	31.4	0.936	0.780

Table 4 summarizes the Faraday probe analysis results. Divergence angle and beam current results are shown for applying versus not applying the extrapolated-wing method. All results beyond the 6th column are derived from applying the extrapolated-wing method. As before, operating conditions with abnormal ExB traces are highlighted with asterisks under the discharge voltage column. The use of the extrapolated-wing approach appears to greatly change both the divergence angle and the beam current. The implication is that the CEX wings are broad as previously seen in the Faraday probe plots. Effective SEE yield varies from 0.06 to 0.09 (possibly more since ExB probe data for some conditions are questionable).

C. Efficiency analysis results

The full physical picture of the NASA-300M will now be studied. Table 5 shows the thrust and the various efficiencies that were calculated during the current study. The probe-derived η_a refers to the anode efficiency derived from the use of probe data with the phenomenological model (Eqs. (29) to (34)). The thrust-derived η_a refers to the anode efficiency calculated from thrust measurement via Eq. (1).

Table 5 shows several signs that indicate the abnormality in the ExB probe traces for the low-voltage, high-current operating conditions is problematic. The mass utilization efficiencies for the 200 V, 50 A and 300 V, 67 A are well above 1 and unphysical; one of the possible causes of these results is the inability of the ExB probe analysis program to properly isolate the peaks associated with the higher charged states, which causes an overestimation of the α_m parameter and the η_m. Another possible culprit is the broad CEX wings present in the Faraday probe traces for these operating conditions. Comparing Figs. 15 and 16 to Figs. 17 and 18, the CEX wings have much higher amplitude relative to the central

Table 5. Summary of thrust measurement and efficiency analysis.
Asterisks in the discharge voltage column indicate conditions with abnormal ExB traces.

Disch. voltage, V	Disch. current, A	Thrust, mN	η_v	η_d	η_b	η_m	η_q	Probe-derived η_a	Thrust-derived η_a	Difference
*200.6	49.8	671	0.873	0.804	0.806	1.198	0.980	0.665	0.565	0.100
300.2	33.5	652	0.926	0.932	0.766	0.969	0.980	0.628	0.654	-0.026
*300.4	50.5	912	0.934	0.901	0.759	1.050	0.974	0.652	0.651	0.001
*301.3	67.8	1161	0.906	0.878	0.776	1.178	0.975	0.709	0.632	0.077
400.1	25.4	581	0.942	0.934	0.777	0.938	0.978	0.627	0.657	-0.031
400.7	37.5	852	0.940	0.937	0.776	0.991	0.976	0.660	0.692	-0.031
400.6	49.8	1099	0.943	0.938	0.768	1.049	0.977	0.696	0.693	0.003
500.3	20.2	528	0.962	0.931	0.795	0.913	0.976	0.634	0.668	-0.034
500.7	30.2	770	0.942	0.931	0.792	0.990	0.979	0.673	0.673	0.000
500.4	40.3	1004	0.959	0.936	0.780	1.018	0.975	0.695	0.686	0.009

peak height for the operating conditions with abnormal ExB probe traces than for those with normal traces. The analyzed data may still contain a non-negligible amount of CEX broadening despite the use of the extrapolated-wing method. The mass utilization efficiency calculated for certain other operating conditions also rises above 1 though they are still physical if one accounts for the uncertainty in the measurement. The fact that the mass utilization efficiency is generally very high may be an indication that the CEX effect on the Faraday probe data is not completely removed. No attempt is made to artificially reduce the mass utilization efficiencies that exceeded 1. If the error sources are truly random, as was assumed in the uncertainty analysis, values that rise above 1 due to random error in one efficiency may be offset by values that are below average in another efficiency. Artificial pruning of the efficiency values can create extra systematic error. As a result of the abnormally high mass utilization efficiency for the 200 V, 50 A and 300 V, 67 A cases, the probe-derived anode efficiency is also abnormally high for those two cases.

Setting aside the low-voltage, high-current operating conditions, we can study Table 5 for trends. Recall the original purpose of the phenomenological model is to provide a means of studying trends and not necessarily to match the thrust-derived anode efficiency. Table 5 shows several trends that have been previously observed for low and medium power Hall thrusters. First, the voltage utilization tends to be higher for higher discharge voltage operation. This is because the voltage needed to extract electrons from the cathode does not vary greatly with the discharge voltage. This extraction voltage takes up an ever smaller fraction of the discharge voltage with increasing discharge voltage.

Second, plume divergence decreases with increasing discharge voltage. Whatever radial voltage drop that is experienced by the ions is likely not varying much with discharge voltage. As a result, the axial voltage drop become more dominant as the discharge voltage increases and the beam becomes more collimated.

Third, mass utilization efficiency appears to rise with mass flow rate. This is expected because the density of the Hall current increases with the discharge current, which increases with the mass flow rate. With that said, given the previously described issues with parts of the ExB probe data and CEX effects on the Faraday probe data, some part of the observed trend may be an artifact of one or both issues.

Fourth, current utilization efficiency and charge utilization efficiency are both fairly constant across all operating conditions. Although this trend is not absolutely certain due to CEX-induced uncertainties, the insensitivity of the charge utilization efficiency to operating condition has been previously observed.[9]

Although the main purpose of the phenomenological model is not to reproduce the thrust-derived anode efficiency, comparison of the anode efficiency provides a good reality check on the results. The last column in Table 5 shows the difference between the probe-derived and the thrust-derived anode efficiencies. With the exception of the operating conditions with abnormal ExB data, the two anode efficiencies agree to within ~4%. Recall the total uncertainty in the thrust-derived anode efficiency is ~4% and the total uncertainty in the probe-derived anode efficiency is ~6%.

V. CONCLUSION

A far-field plume characterization study has been carried out on the NASA-300M. In-depth work on the analysis methods was carried out to identify factors that may have been previously ignored but are important when analyzing the plume of a high-power Hall thruster.

Fresh derivation of the formulas that describe the operation of an ExB probe in the plume of a Hall thruster revealed a new integration approach for calculating current fraction and density fraction. Further study showed that the new integration approach yields the same answer as the old integration approach for a mono-energetic beam. Differences in results between the two approaches are attributed to the different ways the two approaches treat the spread in the particle VDF. Choice of different VDF forms had little effect on the overall results, suggesting that the result is accurate as long as the height and width of the particle distributions are properly captured. While the two integration approaches agree fairly well with each other, they disagree with the peak height approach. Additional analysis show that the CEX correction factor made the biggest difference in the results.

The plume of the NASA-300M is found to carry fairly sizable doubly- and triply-charged populations. Since these higher-charge-state ions have non-negligible SEE yield, a new SEE correction formula for nude Faraday probe is derived from data by Hagstrum.[28-31] This formula predicted an effective SEE yield of 0.06 to 0.09 for the conditions present in the current study.

The trends revealed by the phenomenological model generally agree with past observation on lower power thrusters. When the thruster operates at higher discharge voltages, it tends to utilize more of the discharge voltage and have lower divergence. When the thruster operates at higher mass flow rate, it tends to utilize more of the mass flow. Barring a few conditions with abnormal data, the anode efficiency derived from probe measurements agree with that derived from thrust measurements to within 4%.

From the present study, one can conclude that for high-power Hall thruster plume characterization, extra care must be taken with positioning of the probe. Unlike low-power Hall thruster studies, thruster heating places a demanding constraint on how close to the thruster the ExB probe and RPA can be placed. However, if the probes are too far away, CEX effects can degrade the quality of the probe data (this may have been the cause of the abnormal ExB probe traces). Probe shields, shutters, and possibly even active cooling may become necessary for characterization studies of very-high-power Hall thrusters (50+ kW). For the Faraday probe, the need for the point-source approximation will drive the closest distance to the thruster that the probe can be used. Given the large influence of CEX wings on the analysis results, it is likely that scanning at multiple distances and background pressures may become necessary for obtaining accurate results.

VI. FUTURE WORK

Further work is needed in several areas. Now that the AFRL RPA has been validated, the far-field tower is no longer limited by the usable range of the GRC RPA. Future testing can involve putting the tower closer to the thruster. The ExB probe data may be of higher quality when taken with the probe closer to the thruster.

Given the results of the current study, future work should involve taking Faraday probe data at multiple distances, possibly with multiple background pressures. However, if CEX effects continue to overwhelm the wings of the Faraday probe traces, a gridded Faraday probe may be needed in conjunction with a nude Faraday probe. Such a setup has the added benefit of being able to suppress SEE. For SEE correction of nude Faraday probe data, more research must be carried out to determine a proper value of triply-charged xenon-induced SEE yield.

The next far-field plume characterization test will be carried out on the NASA-300MS, the magnetically shielded version of the NASA-300M. While some of the above changes will be implemented for this next test, others may not be implemented in order to make the results between the two tests comparable.

APPENDIX

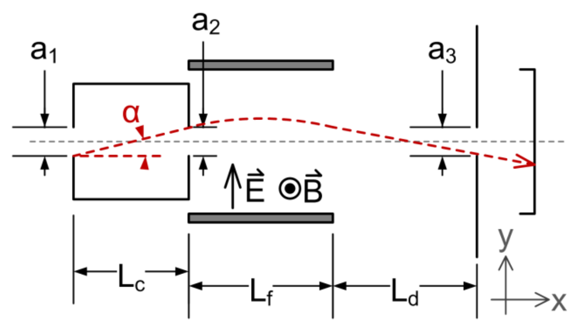

Figure 19. Simplified diagram of a generic ExB probe with drift section.

Derivation of ExB probe resolution begins with an assumption on the geometric design of the ExB probe. Figure 19 shows the design of a generic ExB probe with a drift section. This simplified and exaggerated diagram also represents the ExB probe used for the current study. On the left of the diagram, there is the collimator, which has a circular entrance orifice of diameter a_1, a circular exit orifice of diameter a_2, and a length of L_c. The particle is injected at the maximum collimator acceptance angle, α, and enters the filter section. The filter section is of length L_f and is sufficiently wide that the particle does not hit the bias plates (grey rectangles). The electric and magnetic fields in the particle path are uniform, perpendicular, and of magnitude E_0 and B_0, respectively. The example particle in this derivation is traveling slightly faster than the filter velocity u_0, which is equal to E_0/B_0. The velocity of the particle is assigned to be $u_0+\Delta u$. Because the particle is slightly too fast, it experiences a net downward acceleration in the filter section and passes into the drift section. The drift section is of length L_d. The particle is just slow enough to pass through the circular orifice of diameter a_3 in the SEE suppression plate. The collector is sufficiently large as to collect all ions passing through the orifice on the SEE suppression plate. In some ExB probe designs, an exit collimator replaces the SEE suppression plate. The diameter of the entrance orifice for the exit collimator would become a_3. Two assumptions will be used in this derivation. One, the acceptance angle is small enough that small angle approximation applies. Two, $\Delta u << u_0$, so the equation can be linearized.

Applying the equations of motion to the collimator section, we can obtain Eq. (37) for the acceptance angle of the collimator. Note the use of the small angle approximation.

$$\sin\alpha \approx \tan\alpha = \frac{a_1 + a_2}{2L_c} \tag{37}$$

Applying the equations of motion to the filter section, we obtain Eq. (38) for the x-axis and Eq. (39) for the y-axis. Note the use of the $\Delta u << u_0$ assumption in Eq. (38).

$$\tau_f \approx L_f / u_0 \tag{38}$$

$$\Delta y_f = \tfrac{1}{2}\Delta a \tau_f{}^2 + u_0 \sin\alpha \tau_f \tag{39}$$

$$\Delta u = -\frac{m}{ZeB_0}\Delta a \tag{40}$$

where τ_f is the dwell time of the particle in the filter section, Δy_f is the change in y-position of the particle between where it enters and where it exits the filter section, and Δa is the net acceleration on the particle due to the velocity of the particle deviating from the filter velocity. The relationship between Δu and Δa is derived from force balance in the filter section and shown in Eq. (40). Applying the equations of motion to the drift section, we obtain Eq. (41) for the x-axis and Eq. (42) for the y-axis.

$$\tau_d \approx L_d / u_0 \tag{41}$$

$$\Delta y_d = u_{y,d}\tau_d = \Delta a \tau_f \tau_d + u_0 \sin\alpha \tau_d \tag{42}$$

where τ_d is the dwell time of the particle in the drift section, Δy_d is the change in y-position of the particle between where it enters and where it exits the drift section, and $u_{y,d}$ is the y-velocity of the particle as it enters the drift section. $u_{y,d}$ is calculated from the equations of motion for the filter section. Next, we note that the total change in the y-position of the particle between where it enters the filter section and where it exits the drift section is equal to the negative of the difference in y-position between the upper lip of the collimator exit and the lower lip of the orifice on the SEE suppression plate. This relationship is expressed in Eq. (43).

$$\Delta y_f + \Delta y_d = -\left(\frac{a_2 + a_3}{2}\right) \tag{43}$$

Next, substitute Eqs. (37)-(39), (41), and (42) into Eq. (43) and re-arrange some terms to obtain Eq. (44). Lastly, substituting Eq. (44) into Eq. (40) to obtain an expression for the maximum deviation in velocity that a particle can have and still reach the collector.

$$\Delta a = -\left[\frac{a_2 + a_3 + (a_1 + a_2)(L_f + L_d)/L_c}{L_f^2 + 2L_d L_f}\right] u_0^2 \tag{44}$$

$$\Delta u = \frac{m u_0^2}{ZeB_0}\left[\frac{a_2 + a_3 + (a_1 + a_2)(L_f + L_d)/L_c}{L_f^2 + 2L_d L_f}\right] \tag{45}$$

Note, if the acceptance angle of the ExB probe is larger than the angle subtended by the plasma source, the angle α is no longer the limiting parameter. Instead, the angle β (Eq. (46)) should be used and the form of Eq. (45) changes to Eq. (47).

$$\sin\beta \approx \frac{D_{PS}}{2R_{ExB}} \tag{46}$$

$$\Delta u = \frac{m u_0^2}{ZeB_0}\left[\frac{a_2 + a_3 + 2\sin\beta(L_f + L_d)}{L_f^2 + 2L_d L_f}\right] \tag{47}$$

where D_{PS} is the diameter of the plasma source and R_{ExB} is the distance between the ExB probe and the plasma source. For the probe used in this study, the acceptance angle is sufficiently small that Eq. (47) does not apply.

For an ExB probe without a drift section, we can set L_d to 0 in Eq. (45), which simplifies into Eq. (48).

$$\Delta u = \frac{m u_0^2}{ZeB_0}\left[\frac{a_2 + a_3 + (a_1 + a_2) * L_f / L_c}{L_f^2}\right] \tag{48}$$

By comparing Eq. (48) to Eq. (45), one can see that the addition of the drift section will generally improve the resolution of the ExB probe. Note that a_1, a_2, a_3, L_c, L_f, L_d, and R_{ExB} are all geometric constants for a given experimental setup. D_{PS} is also typically a constant (though one can never be too careful when generalizing about plasma sources). A scaling equation for the maximum accepted deviation in velocity of a generic ExB probe, shown in Eq. (49), can now be written.

$$\Delta u = \frac{m u_0^2}{ZeB_0} G \tag{49}$$

where G is a geometric constant.

Here are some quick observations about the maximum accepted deviation in velocity for an ExB probe. One, the numerator of Eq. (49) contains the ion kinetic energy while the denominator contains the ion charge. In other words, Δu scales with the ion energy per charge of the incoming particles, which is slightly lower than the discharge voltage of a Hall thruster. The implication of this trend for a Hall thruster is that Δu is species-insensitive because all charged species undergo similar voltage drop and have similar ion energy per charge. When calculating ExB probe resolution as a relative percentage, the value for the singly-charged species will always be the biggest. That is because Δu is roughly constant while u_0 increases with species charge.

Two, dividing both sides of Eq. (49) by u_0, we obtain Eq. (50).

$$\frac{\Delta u}{u_0} = \frac{mu_0}{ZeB_0} G \tag{50}$$

This equation says that for a given charged species, the ExB probe resolution in relative percentage increases with the velocity of the particle. For instance, an ExB probe with a ±2% resolution when probing the plume of a 250-V thruster would have a ±4% resolution when probing the plume of a 1000-V thruster. The probe resolution in relative percentage scales as the velocity of the particles, which scale as the square root of the accelerating voltage. This is perhaps part of the reason why ExB probe traces for ion thruster are never able to resolve the VDF of the plume particles. The high accelerating voltage (1000+ V) associated with an ion thruster means Δu will generally be large. The combination of low VDF spread and large Δu means that Δu is generally larger than the VDF spread for an ion thruster. This interesting trend also means that an ExB probe used to interrogate the plume of a Hall thruster operating at high discharge voltage should have tight dimensions to ensure Δu is several times smaller than the width of the ion VDF.

ACKNOWLEDGMENTS

We thank the NASA Space Technology Mission Directorate In-Space Propulsion project for funding this work, and Timothy D. Smith for managing the work. We acknowledge David M. Manzella, David T. Jacobson, and Robert S. Jankovsky for the design and fabrication of the NASA-457Mv2 Hall thruster, and Peter Peterson and Christopher Griffith for the design of the NASA-300M Hall thruster. We acknowledge Thomas Haag for work on the thrust stand and Daniel L. Brown and Joseph Blakely of the Air Force Research Laboratory for their retarding potential analyzer. And we acknowledge Kevin L. Blake, George W. Readus, and George P. Jacynycz for the thruster fabrication, assembly of the test setup, and operation of the vacuum facility.

REFERENCES

1. ***NASA Exploration Systems Mission Directorate Presentation, Human Space Exploration Summary***, http://www.nasa.gov/exploration/new_space_enterprise/home/heft_summary.html, Jan., 2011.

2. Mercer, C. R., et al., ***Benefits of Power and Propulsion Technology for a Piloted Electric Vehicle to an Asteroid*** 47th AIAA/ASME/SAE/ASEE Joint Propulsion Conference & Exhibit, AIAA-2011-7252, San Diego, CA, 31 Jul.- 3 Aug., 2011.

3. Capadona, L. A., et al., ***Feasibility of Large High-Powered Solar Electric Propulsion Vehicles: Issues and Solutions***, 47th AIAA/ASME/SAE/ASEE Joint Propulsion Conference & Exhibit, AIAA-2011-7251, San Diego, CA, 31 Jul.- 3 Aug., 2011.

4. Brophy, J. R., et al., ***300-kW Solar Electric Propulsion System Configuration for Human Exploration of Near-Earth Asteroids***, 47th AIAA/ASME/SAE/ASEE Joint Propulsion Conference & Exhibit, AIAA-2011-5514, San Diego, CA, 31 Jul.- 3 Aug., 2011.

5. Hofer, R. R. and Randolph, T. M., ***Mass and Cost Model for Selecting Thruster Size in Electric Propulsion Systems***, 47th AIAA/ASME/SAE/ASEE Joint Propulsion Conference & Exhibit, AIAA-2011-5518, San Diego, CA, 31 Jul.- 3 Aug., 2011.

6. Kamhawi, H., Haag, T. W., Jacobson, D. T., and Manzella, D. H., ***Performance Evaluation of the NASA-300M 20 kW Hall Effect Thruster***, 47th AIAA/ASME/SAE/ASEE Joint Propulsion Conference & Exhibit, AIAA-2011-5521, San Diego, CA, 31 Jul.- 3 Aug., 2011.

7. Brown, D. L. and Gallimore, A. D., ***Evaluation of Ion Collection Area in Faraday probes***, Review of Scientific Instruments, Vol. 81, No. 6, p. 063504, doi:10.1063/1.3449541, 25 Jun., 2010.

8. Reid, B. M., ***The Influence of Neutral Flow Rate in the Operation of Hall Thrusters***, Ph.D. Dissertation, Aerospace Engineering, University of Michigan, Ann Arbor, MI, 2008.

9. Shastry, R., Hofer, R. R., Reid, B. M., and Gallimore, A. D., ***Method for analyzing ExB probe spectra from Hall thruster plumes***, Review of Scientific Instruments, Vol. 80, No. 6, p. 063502, doi:10.1063/1.3152218, 22 Jun., 2009.

10. Manzella, D. M., ***Scaling Hall Thrusters to High Power***, Ph.D. Dissertation, Mechanical Engineering, Stanford University, Stanford, CA, 2005.

11. Hofer, R. R., Peterson, P. Y., Gallimore, A. D., and Jankovsky, R. S., ***A High Specific Impulse Two-Stage Hall Thruster with Plasma Lens Focusing***, 27th International Electric Propulsion Conference, IEPC-2001-036, Pasadena, CA, 15-19 Oct., 2001.
12. Hofer, R. R. and Gallimore, A. D., ***The Role of Magnetic Field Topography in Improving the Performance of High-Voltage Hall Thrusters***, 38th AIAA/ASME/SAE/ASEE Joint Propulsion Conference & Exhibit, AIAA-2002-4111, Indianapolis, IN, 7-10 Jul., 2002.
13. Haag, T. W., ***Thrust stand for high-power electric propulsion devices***, Review of Scientific Instruments, Vol. 62, No. 5, p. 1186, doi:10.1063/1.1141998, May, 1991.
14. Brown, D. L., ***Investigation of Flow Discharge Voltage Hall Thruster Characteristics and Evaluation of Loss Mechanisms***, Ph.D. Dissertation, Aerospace Engineering, University of Michigan, Ann Arbor, MI, 2009.
15. Lieberman, M. A. and Lichtenberg, A. J., ***Electrostatic Probe Diagnostics***, in Principles of Plasma Discharges and Materials Processing, 2nd ed., Ch., p. 185-203, doi:10.1002/0471724254, Wiley, New York, 2005.
16. Savitzky, A. and Golay, M. J. E., ***Smoothing and Differentiation of Data by Simplified Least Squares Procedures***, Analytical Chemistry, Vol. 36, No. 8, p. 1627-1639, doi:10.1021/ac60214a047, Jul., 1964.
17. Steinier, J., Termonia, Y., and Deltour, J., ***Comments on Smoothing and Differentiation of Data by Simplified Least Squares Procedure***, Analytical Chemistry, Vol. 44, No. 11, p. 1906-1909, doi:10.1021/ac60319a045, Sep., 1972.
18. Hutchinson, I. H., ***Principles of Plasma Diagnostics***, 2nd ed., doi:10.1017/CBO9780511613630, Cambridge University Press, 2002.
19. Hofer, R. R., ***Development and Characterization of High-Efficiency, High-Specific Impulse Xenon Hall Thrusters***, Ph.D. Dissertation, Aerospace Engineering, University of Michigan, Ann Arbor, MI, 2004.
20. Peterson, P. Y., ***The Development and Characterization of a Two-Stage Hybrid Hall/Ion Thruster***, Ph.D. Dissertation, Aerospace Engineering, University of Michigan, Ann Arbor, MI, 2004.
21. Beal, B. E., ***Clustering of Hall Effect Thrusters for High-Power Electric Propulsion Applications***, Ph.D. Dissertation, Aerospace Engineering, University of Michigan, Ann Arbor, MI, 2004.
22. Linnell, J. A., ***An Evaluation of Krypton Propellant in Hall Thrusters***, Ph.D. Dissertation, Aerospace Engineering, University of Michigan, Ann Arbor, MI, 2007.
23. Kim, S.-W., ***Experimental Investigations of Plasma Parameters and Species-Dependent Ion Energy Distribution in the Plasma Exhaust Plume of a Hall Thruster***, Ph.D. Dissertation, Aerospace Engineering, University of Michigan, Ann Arbor, MI, 1999.
24. Kim, V., ***Main physical features and processes determining the performance of stationary plasma thrusters***, Journal of Propulsion and Power, Vol. 14, No. 5, p. 736-743, 1998.
25. Brown, D. L. and Gallimore, A. D., ***Evaluation of Facility Effects on Ion Migration in a Hall Thruster Plume***, Journal of Propulsion and Power, Vol. 27, No. 3, p. 573-585, doi:10.2514/1.B34068, May-Jun, 2011.
26. Huang, W., Kamhawi, H., and Shastry, R., ***Farfield Ion Current Density Measurements before and after the NASA HiVHAc EDU2 Vibration Test***, 48th AIAA/ASME/SAE/ASEE Joint Propulsion Conference & Exhibit, AIAA-2012-4195, Atlanta, GA, 29 Jul.- 1 Aug., 2012.
27. Reid, B. M. and Gallimore, A. D., ***Near-field Ion Current Density Measurements of a 6-kW Hall Thruster***, 31st International Electric Propulsion Conference, 2009-124, Ann Arbor, MI, 20-24 Sep., 2009.
28. Hagstrum, H. D., ***Auger Ejection of Electrons from Tungsten by Noble Gas Ions***, Physical Review, Vol. 96, No. 2, p. 325-335, doi:10.1103/PhysRev.96.325, 15 Oct., 1954.
29. Hagstrum, H. D., ***Auger Ejection of Electrons from Molybdenum by Noble Gas Ions***, Physical Review, Vol. 104, No. 3, p. 672-683, doi:10.1103/PhysRev.104.672, 1 Nov., 1956.
30. Hagstrum, H. D., ***Auger Ejection of Electrons from Tungsten by Noble Gas Ions***, Physical Review, Vol. 104, No. 2, p. 317-318, doi:10.1103/PhysRev.104.317, 15 Oct., 1956.
31. Hagstrum, H. D., ***Metastable Ions of the Noble Gases***, Physical Review, Vol. 104, No. 2, p. 309-316, doi:10.1103/PhysRev.104.309, Sep., 1956.
32. Hofer, R. R. and Gallimore, A. D., ***High-Specific Impulse Hall Thrusters, Part 2: Efficiency Analysis***, Journal of Propulsion and Power, Vol. 22, No. 4, p. 732-740, doi:10.2514/1.15954, Jul.-Aug., 2006.

Farfield Plume Measurement and Analysis on the NASA-300M

Wensheng Huang, Rohit Shastry, George C. Soulas, Hani Kamhawi

NASA Glenn Research Center

Present at 60th JANNAF Propulsion meeting, Colorado Springs, May 1, 2013

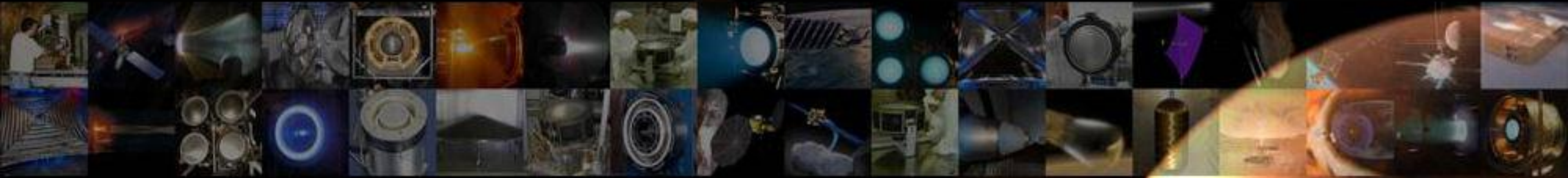

Introduction (1/2)

- NASA Space Technology Mission Directorate (STMD) is investing in the development of a 15-kW Hall thruster,
  - Stepping stone toward higher power system for human exploration
  - Provide propulsion system for Solar Electric Propulsion Technology Demonstration Mission (SEP TDM), which demo SotA solar array, electric propulsion, and associated spacecraft technologies.
- NASA GRC and JPL jointly developing high-power magnetically-shielded Hall thruster via combined experiment-simulation approach

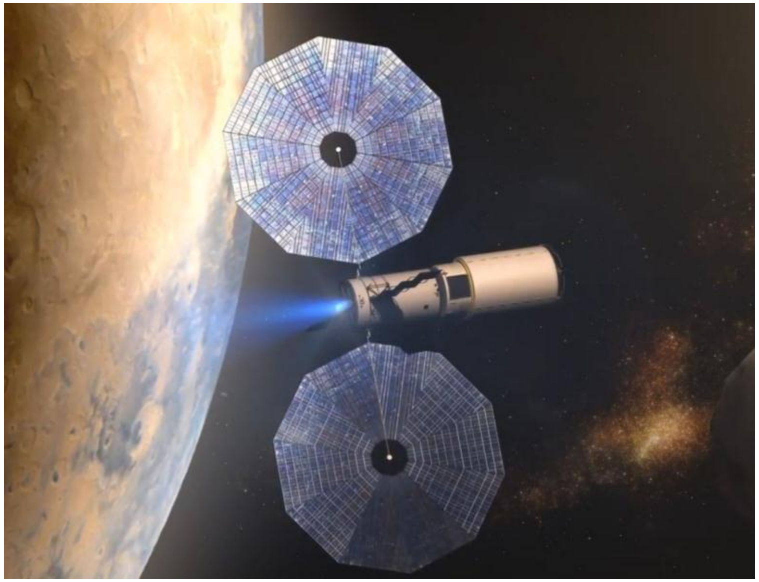

Introduction (2/2)

- To guide development, a magnetically-shield version of the NASA-300M called NASA-300MS will be built and tested
- Experimental work include extensive far-field, near-field, and interior probing.
- The present work covers the far-field plume characterization of the 300M, which will serve as a baseline for comparison to the 300MS

NASA-300M

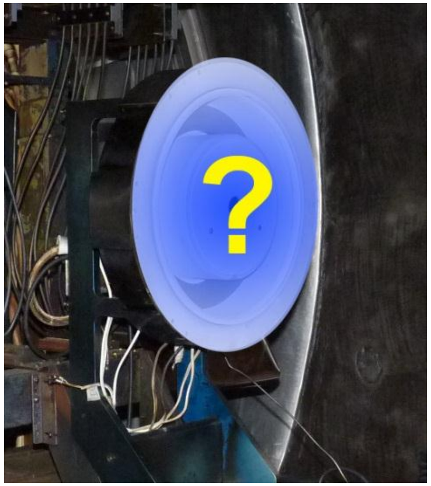

NASA-300MS

Outline

- Introduction
- Experimental Setup
- Data Analysis
    - New integration formula for ExB probe analysis
    - Effects of SEE for far-field Faraday probe
- Results
- Future Works and Conclusion

NASA-300M Hall thruster

- NASA-300M is a 20-kW Hall thruster:
  - Magnetic lens topology, symmetric about channel centerline,
  - Magnetic field strength optimized for anode efficiency
  - Centrally-mounted cathode, 8% CFF
  - Nominal operating condition: 500 V, 40 A
- 10 conditions tested
  - Discharge power: 10, 15, 20 kW
  - Discharge voltage: 200 - 500 V
  - Discharge current: 20 - 67 A
  - Thrust: 530 - 1160 mN
  - Anode efficiency: 57 – 69 %
- Tested in VF5
- 7 ion gauges to monitor pressure
  - Pressure near thruster < 3e-5 Torr

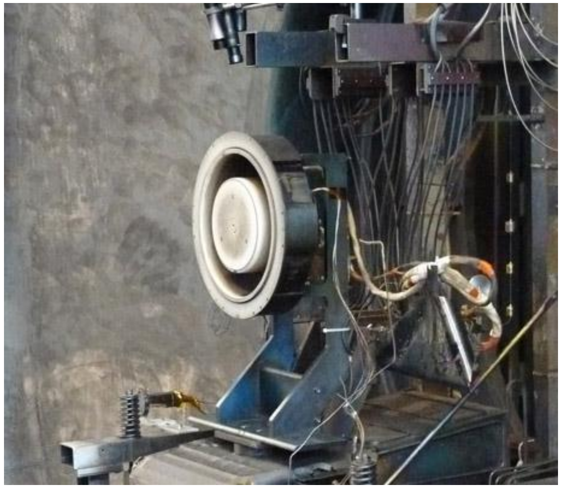

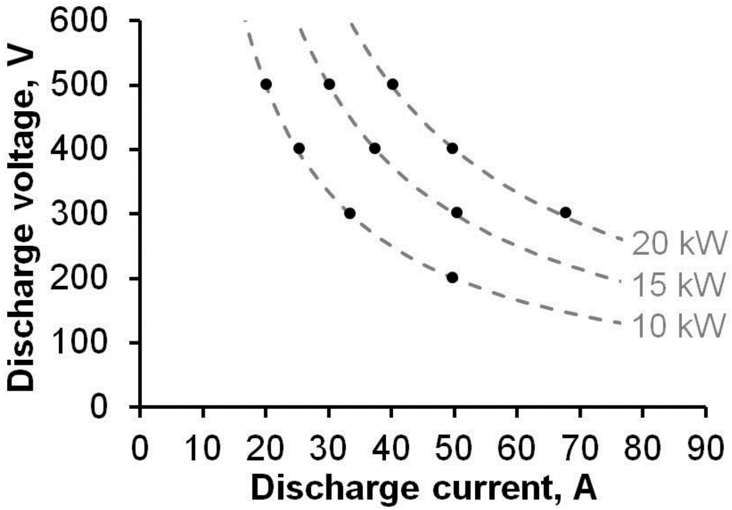

Setup: Facility and motion system

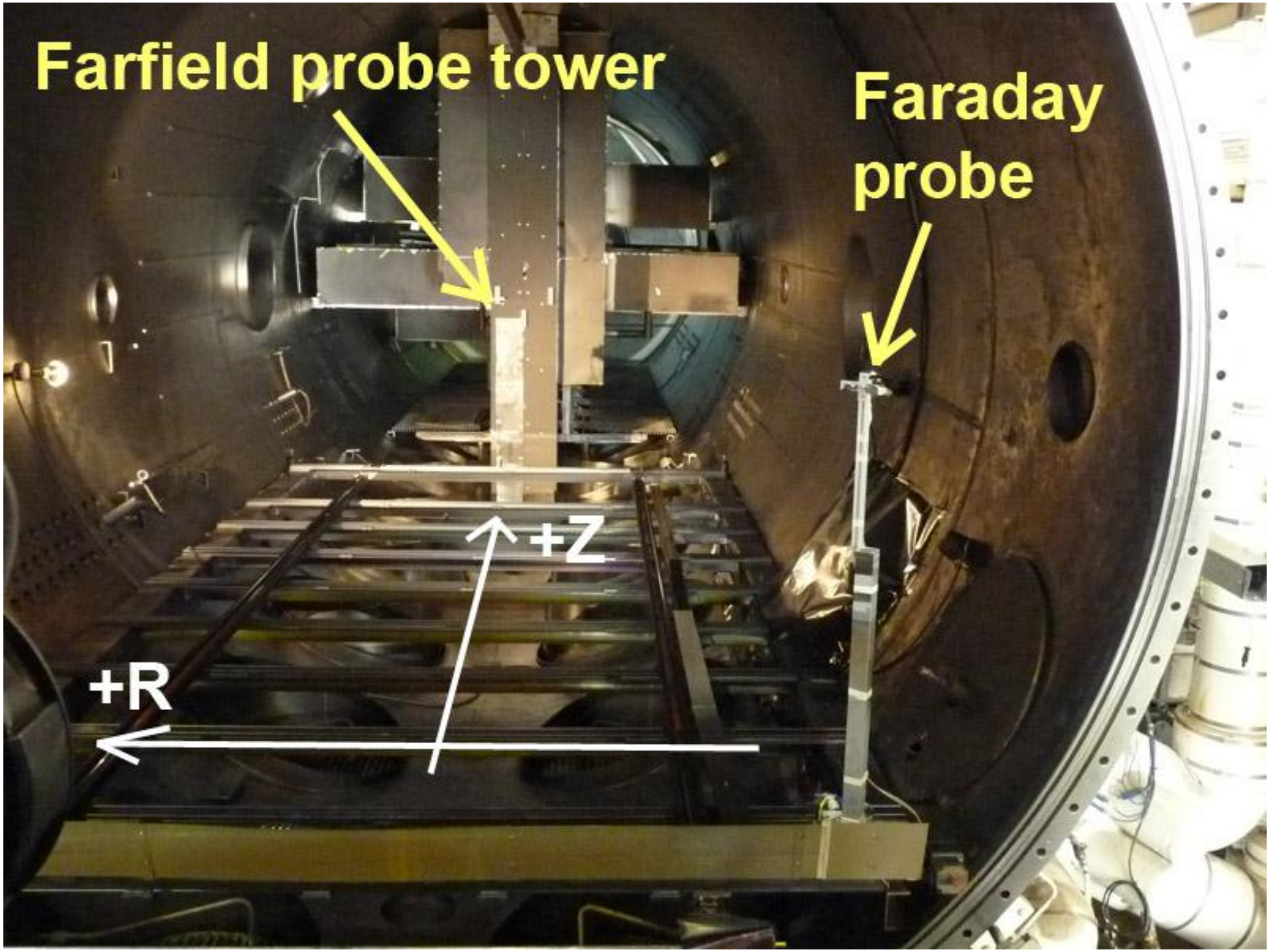

Setup: Probes

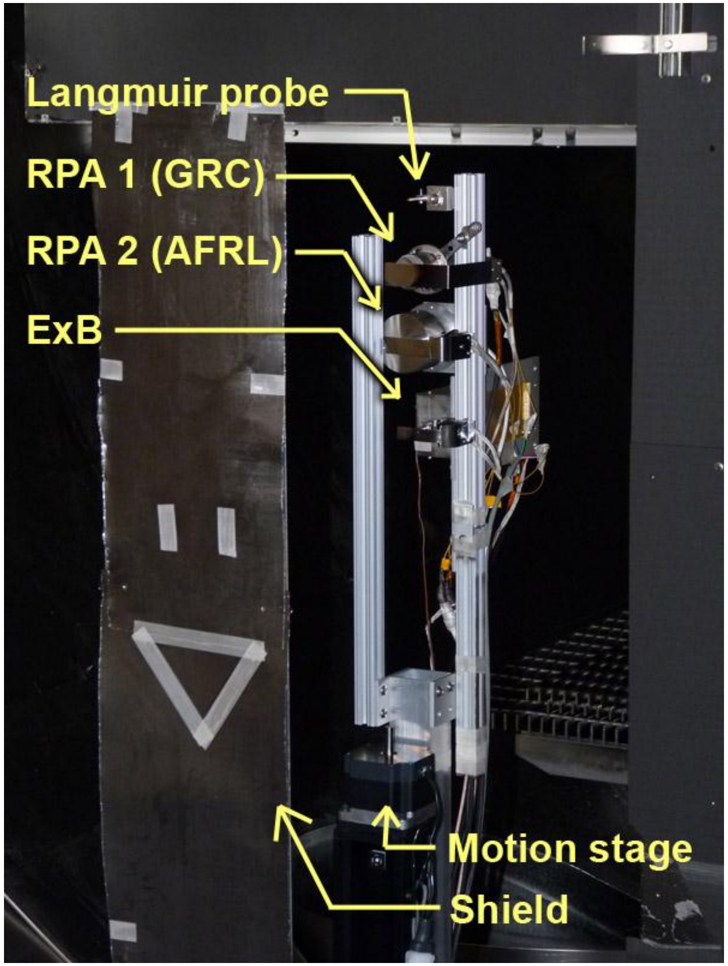

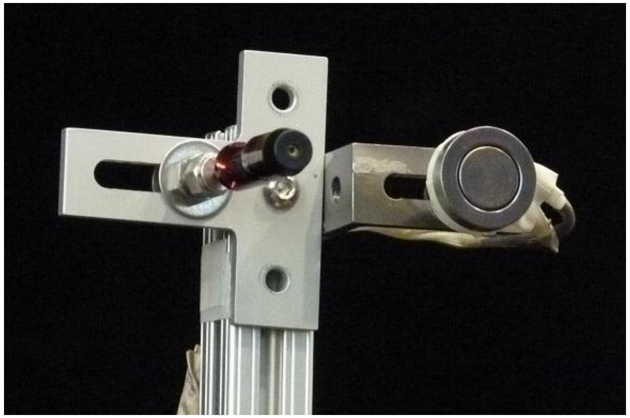

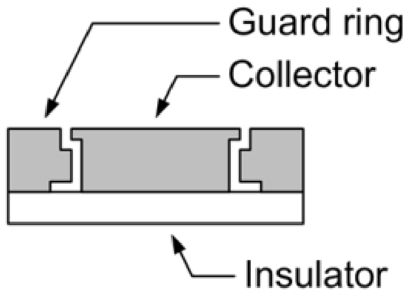

- Probe tower at ~27 MTD
  - RPA 1, GRC design, cannot be placed closer than 25 MTD
  - RPA 2, new AFRL design
  - ExB, commercial
- FP polarly-swept at 5 MTD

Data analysis:
Langmuir probe and RPA

- Langmuir probe analysis: simple Langmuir probe theory
  - 20 traces per test point, averaged and then smoothed
  - Plotted derivative of probe current with respect to probe voltage
  - Peak-amplitude voltage is plasma potential

- RPA analysis:
  - The trace is smoothed
  - Plot -dC/dV versus RPA bias voltage
  - Traditionally, take the most probable voltage as the ion energy per charge
  - For this study, took ensemble average of the part of the peak that exceeded 50% of max amplitude

RPA Analysis plot, 200V, 50 A ▶

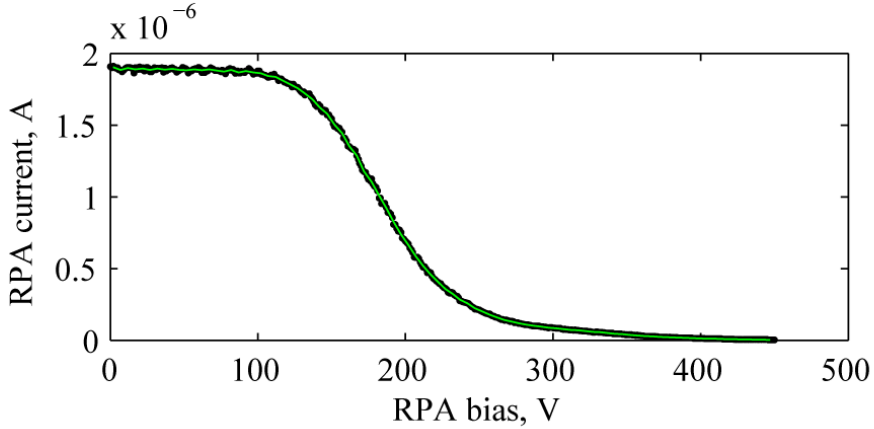

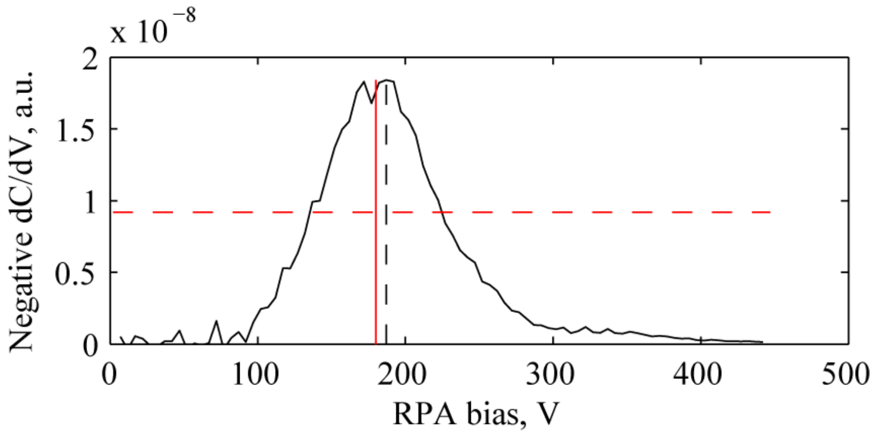

Data analysis:
ExB probe

- Traditional approach involves fitting the species peaks in the collector current versus bias voltage plot to various equation forms and calculating the area under the curve
- New approach is very similar except the integration is carried out using <u>new integration formulas</u> that were vigorously derived
- Steps for analysis of ExB probe data:
  1. Determine rough locations of the peaks
  2. Choose curve-fit boundaries
     - 1/3 of the way to the next peak on left, 1.5X peak location on right
  3. Perform curve-fit using the chosen VDF form
  4. Integrate the fitted curve using the new integration formulas to obtain raw current and species fractions
  5. Correct for CEX attenuation
     - CEX model require background neutral density (from ion gauges),
     - and average ion energy per charge (from RPA)

Data analysis:
ExB probe – VDF forms

- Tried four VDF forms
  - Triangle: $$f_j(u) = \begin{cases} (-a/b)*\left|u-c\right|+a, & c-b<u<c+b \\ 0, & \text{else} \end{cases}$$
  - Gaussian: $$f_j(u) = a*\exp[-b(u-c)^2]$$
  - Variable exponent: $$f_j(u) = a*\exp[-b\left|u-c\right|^n]$$
  - Twin Gaussian: $$f_j(u) = a_1*\exp[-b_1(u-c_1)^2]+a_2*\exp[-b_2(u-c_2)^2]$$
- Perform curve-fit using this equation (insert f_j from above):

$$I_{P,j}(V_P) = K_1 n_j V_P^{\,3} f_j(K_2 V_P)$$

- Then use these formulas for species and current fractions:

$$\zeta_j \equiv \frac{n_j}{\sum_k n_k} = \frac{\int_0^\infty \frac{I_{P,j}(V_P)}{V_P^{\,3}} dV_P}{\sum_k \int_0^\infty \frac{I_{P,k}(V_P)}{V_P^{\,3}} dV_P} \qquad \Omega_j \equiv \frac{I_j}{\sum_k I_k} = \frac{Z_j \int_0^\infty \frac{I_{P,j}(V_P)}{V_P^{\,2}} dV_P}{\sum_k Z_k \int_0^\infty \frac{I_{P,k}(V_P)}{V_P^{\,2}} dV_P}$$

- Integrating area under the curve is equivalent to:

$$\Omega_j \equiv \frac{I_j}{\sum_k I_k} \approx \frac{\int_0^\infty I_{P,j}(V_P)\, dV_P}{\sum_k \int_0^\infty I_{P,k}(V_P)\, dV_P}$$

*Derivations for all equations shown in paper.

Data analysis:
ExB probe – curve fit (1/2)

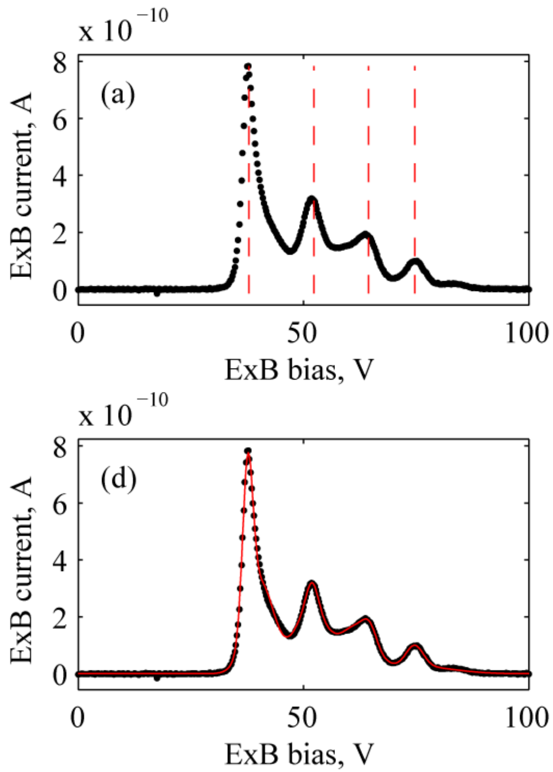

- Black dot = data point
- Vertical dashed line = peak locations
- Red line = sum of curve-fits

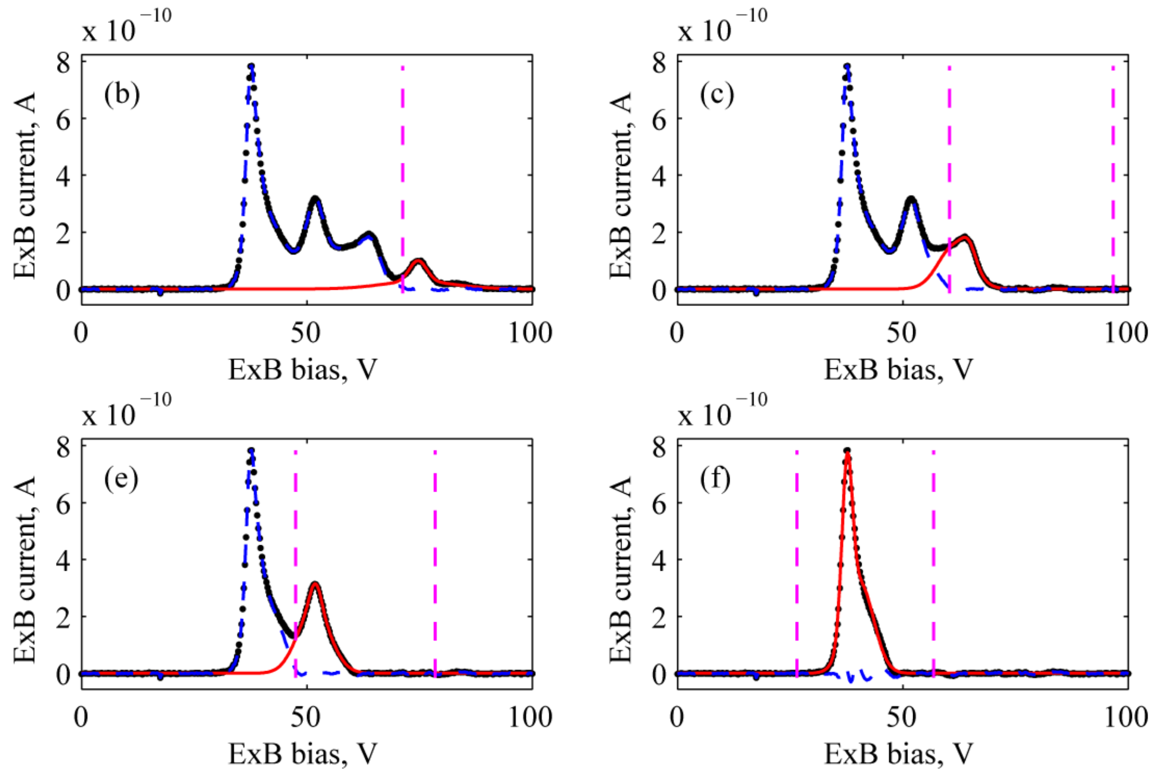

- Black dot = data point
- Red line = curve fit
- Blue dashed line = left-over
- Pink vertical line = curve-fit boundaries

Data analysis:
ExB probe – curve fit (2/2)

Triangle form

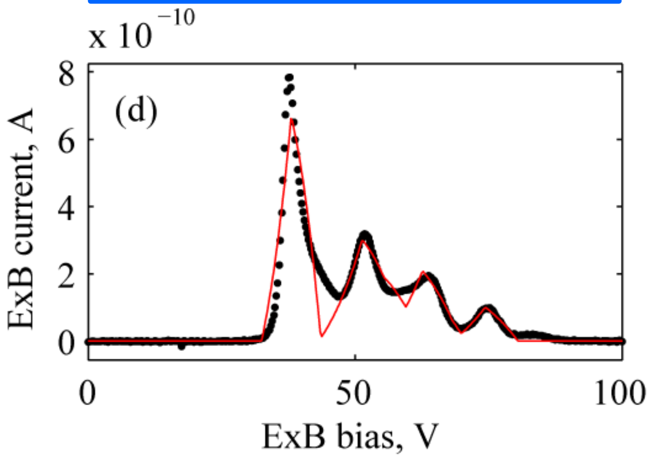

Gaussian form

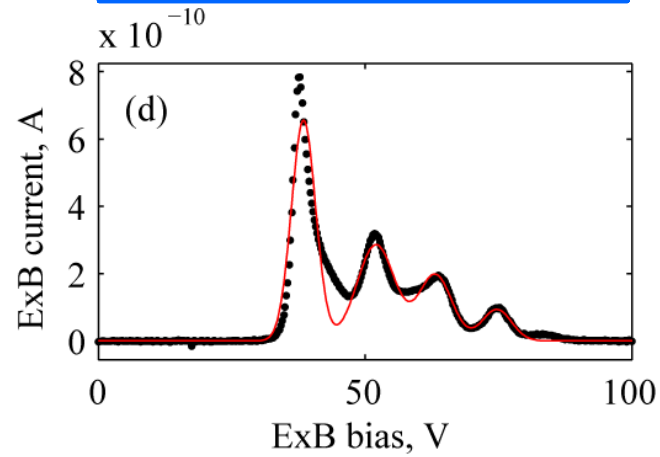

Variable exponent form

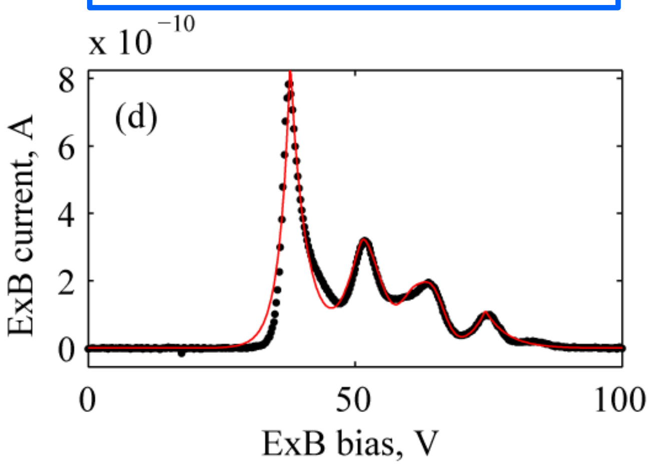

Twin Gaussian form

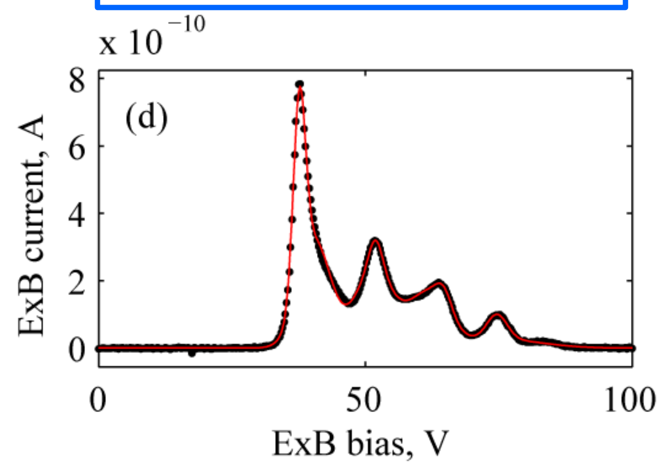

Data analysis: Faraday probe

- Assumptions:
  - Plume is axisymmetric
  - Constant charge-state ratio
- Charge-weighted divergence angle equation for polar sweep:

$$< \cos\delta >= \frac{2\pi R_{FP}{}^2 \int_0^{\pi/2} j(\theta)\cos\theta\sin\theta\, d\theta}{2\pi R_{FP}{}^2 \int_0^{\pi/2} j(\theta)\sin\theta\, d\theta}$$

- Denominator equal to total ion beam current
- <u>Extrapolated-wing</u> to counter effects of CEX

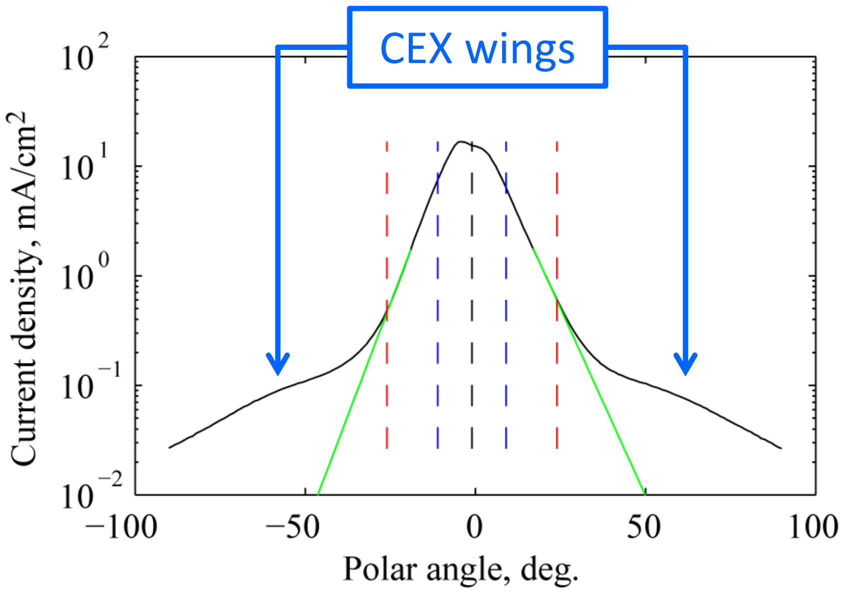

Data analysis:
Faraday probe – SEE effects

- SEE effects are negligible if plume consist mostly of singly-charged ions, which is not true for this study
- Data for Xe^+, Xe^{2+} yield from experiments by Hagstrum; Data for Xe^{3+} yield extrapolated from said experiments*
- Figure from Hagstrum's work*

Bombarding particle	SEE yield of molybdenum
Xe^+	0.022
Xe^{2+}	0.20
Xe^{3+}	0.70

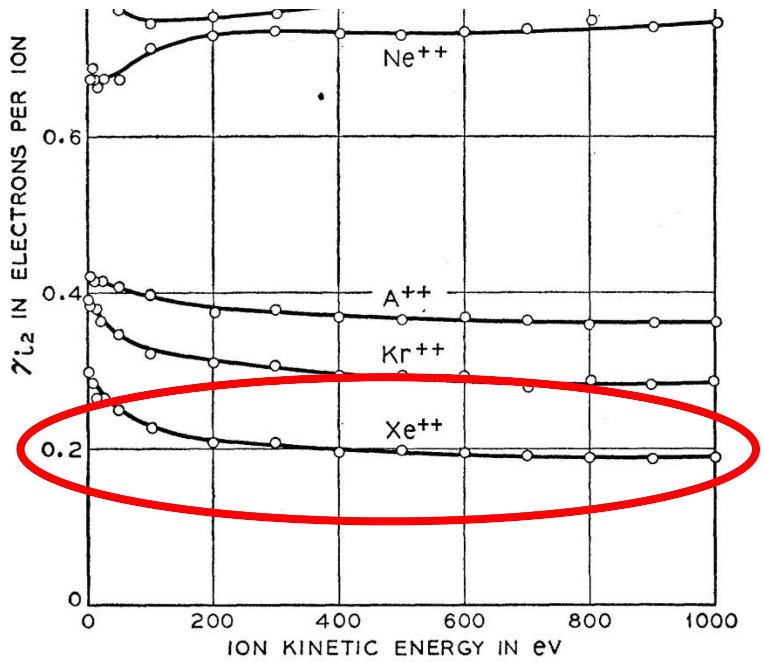

$$J = \frac{J_{FP}}{1+\gamma_{eff}} = J_{FP} * \sum_k \frac{\Omega_k}{1+\gamma_k}$$

- Equation above used to correct SEE effects,
  - γ_{eff} = effective SEE yield for given charged species composition; **0.06** to **0.09** for the present study

*Hagstrum, Phys. Rev., Vol.104, No.3, p.672; Hagstrum, Phys. Rev., Vol.96, No.2, p.325

Data analysis: Phenomenological efficiency model

- A phenomenological efficiency model is used to help study trends:

$$\eta_a = \frac{T^2}{2\dot{m}_a P_d} = \eta_q \eta_v \eta_d \eta_b \eta_m$$

Charge utilization: $\eta_q = \left(\sum_k \frac{\Omega_k}{\sqrt{Z_k}} \right)^2 \Big/ \sum_k \frac{\Omega_k}{Z_k}$

Voltage utilization: $\eta_v = 1 - \frac{V_L}{V_d}$

Plume divergence: $\eta_d = (< \cos\delta >)^2$

Current utilization: $\eta_b = \frac{I_b}{I_d}$

Mass utilization: $\eta_m = \frac{M_{xe} I_b}{\dot{m}_a e} \sum_k \frac{\Omega_k}{Z_k}$

T = thrust
$\dot{m}_a$ = anode mass flow rate
P_d = discharge power
Ω_k = k-th species current fraction
Z_k = k-th species charge state
V_L = loss voltage
V_d = discharge voltage
δ = divergence angle
I_b = total ion current
I_d = discharge current
M_{xe} = mass of xenon atom
e = elementary charge

Results: Abnormal ExB traces

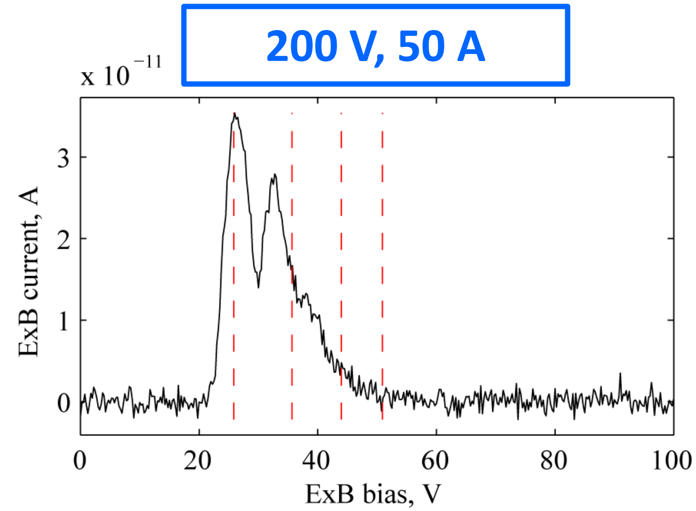

- Higher charge species could not be isolated from lower charge species
- Analysis still carried out the same way
- Uncertainties expected to be high

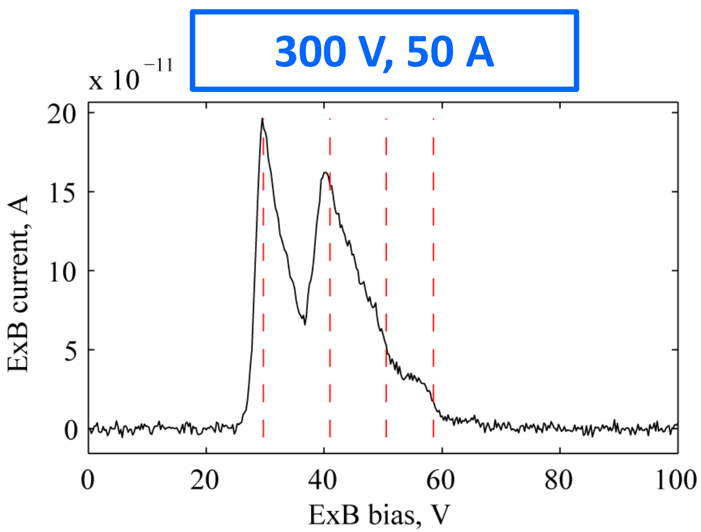

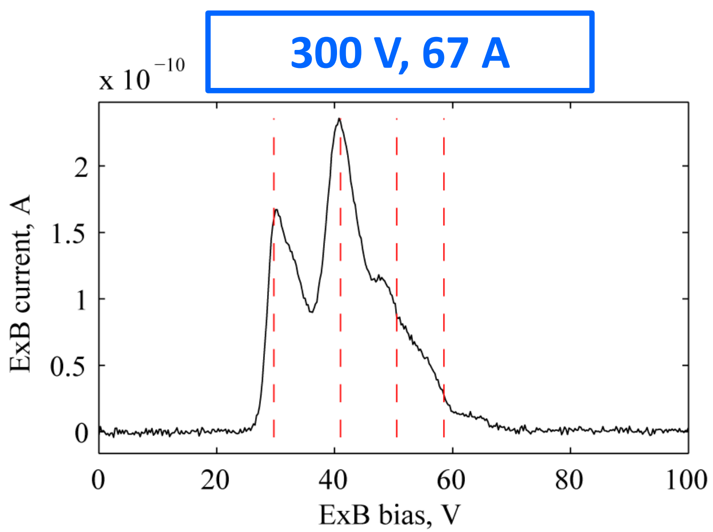

Results: ExB results

- Comparison made using α_m, which is a term in η_m -> $\alpha_m = \sum_k \frac{\Omega_k}{Z_k}$
- On the average, new integration approach ~1% less than old
  - Turns out they are equal for mono-energetic beam (derived in paper)
  - Difference is due to difference in treatment of VDF spread
- Different VDF forms gave roughly the same results
  - Exact shape not important if height and width properly captured

Integration approach	VDF form	Corrected for CEX	Average relative difference in α_m	Std. dev. of relative difference in α_m
New	Twin Gaussian	Yes	Baseline	-
New	Triangle	Yes	-0.26%	0.64%
New	Gaussian	Yes	-0.51%	0.60%
New	Variable exponent	Yes	1.27%	0.57%
Old	Twin Gaussian	Yes	1.80%	0.50%
Old	Triangle	Yes	0.38%	0.71%
Old	Gaussian	Yes	0.52%	0.72%
Old	Variable exponent	Yes	1.21%	0.77%
-	Peak height	Yes	5.66%	0.92%
New	Twin Gaussian	No	-17.0%	4.5%
-	Peak height	No	-7.1%	4.7%

▲Only ExB probe traces that are not abnormal are used

Results: Efficiency Analysis

- Asterisk in discharge voltage column indicate conditions with abnormal ExB traces
  - 2 of 3 shows abnormally high mass utilization (in orange)
- η_v and η_d increase with discharge voltage
- η_m increase with anode mass flow rate

Disch. voltage, V	Disch. current, A	Thrust, mN	η_v	η_d	η_b	η_m	η_q	Probe-derived η_a	Thrust-derived η_a	Difference
*200.6	49.8	671	0.873	0.804	0.806	1.198	0.980	0.665	0.565	0.100
300.2	33.5	652	0.926	0.932	0.766	0.969	0.980	0.628	0.654	-0.026
*300.4	50.5	912	0.934	0.901	0.759	1.050	0.974	0.652	0.651	0.001
*301.3	67.8	1161	0.906	0.878	0.776	1.178	0.975	0.709	0.632	0.077
400.1	25.4	581	0.942	0.934	0.777	0.938	0.978	0.627	0.657	-0.031
400.7	37.5	852	0.940	0.937	0.776	0.991	0.976	0.660	0.692	-0.031
400.6	49.8	1099	0.943	0.938	0.768	1.049	0.977	0.696	0.693	0.003
500.3	20.2	528	0.962	0.931	0.795	0.913	0.976	0.634	0.668	-0.034
500.7	30.2	770	0.942	0.931	0.792	0.990	0.979	0.673	0.673	0.000
500.4	40.3	1004	0.959	0.936	0.780	1.018	0.975	0.695	0.686	0.009

Future Work

- Try to take ExB probe data closer to thruster to see if the abnormal traces become normal
- CEX effects on Faraday probe trace may have made η_m too high, need to take data at multiple distances and background pressures
- Try to find the true value of triply-charged xenon-induced SEE yield of molybdenum
- Perform similar tests on the NASA-300MS

Conclusion

- New derivation of ExB probe analysis revealed a new formula for integration
  - The result is roughly equal to integrating the area under the curve (old approach) for the present data set
- Comparison between four different VDF forms suggest the exact form does not matter as long as the height and width are captured
- Found a formula for offsetting the effects of secondary electron emission from a Faraday probe
  - For this study, 6-9% effect on total ion current
- Really need to take data at multiple distances and pressure to correct for CEX effects on Faraday probe data
- Overall, this 20-kW Hall thruster have similar physical trends as lower power thrusters
  - η_v and η_d increase with discharge voltage
  - η_m increase with anode mass flow rate

Acknowledgment

- We thank,
  - The NASA Space Technology Mission Directorate In-Space Propulsion (STMD ISP) project for funding this work,
  - Timothy D. Smith for managing the work,
  - Peter Peterson and Christopher Griffith for the design of the NASA-300M Hall thruster,
  - Thomas Haag for work on the thrust stand,
  - Daniel L. Brown and Joseph Blakely of the Air Force Research Laboratory for their retarding potential analyzer,
  - And Kevin L. Blake, George W. Readus, and George P. Jacynycz for thruster fabrication, aid with test setup, and operation of the vacuum facility.

Questions